SAPIENZA
Università di Roma

PhD Programme in Life Sciences

XXXV Cycle

Microglia reactivity entails microtubule remodeling from acentrosomal to centrosomal arrays

Candidate
Caterina Sanchini
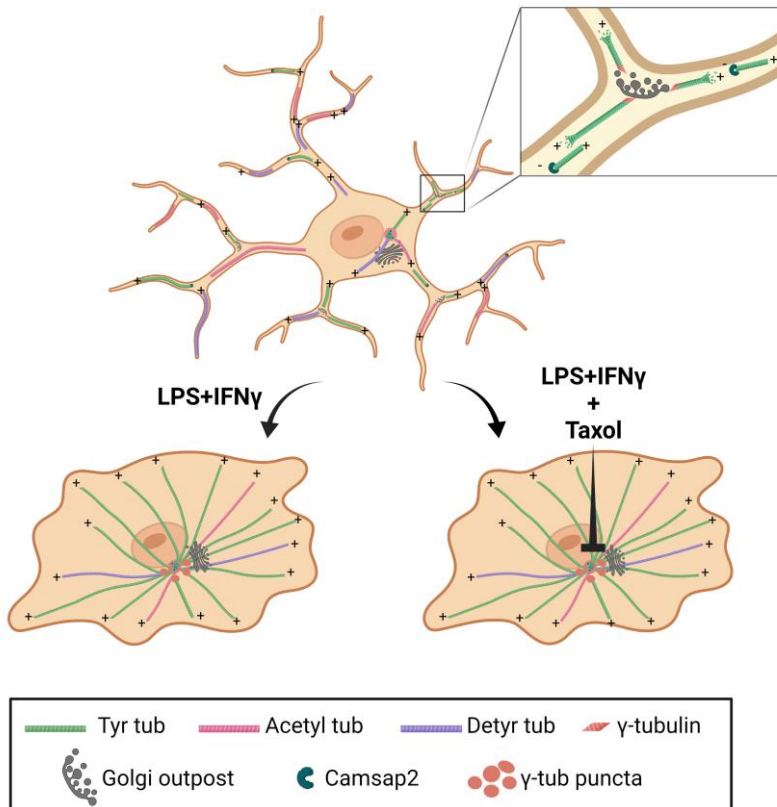
Supervisor
Prof. Silvia Di Angelantonio

Tutor
Dr. Maria Rosito

Coordinator
Prof. Francesca Cutruzzolà

Index

Graphical abstract

Graphical abstract to illustrate the main findings of this study. Homeostatic microglia have stable microtubule arrays, represented by higher levels of acetylated (Acetyl tub) and detyrosinated (Detyr tub) tubulin. Homeostatic microglia display non-centrosomal microtubules, nucleated at Golgi outposts, with a mixed polarity. Microglia classical activation (with LPS+IFNγ) increases microtubule dynamicity and entails a microtubule cytoskeleton reorganization into a radial array, with increased pericentrosomal material and γ-tubulin localization to puncta around the centrosome, acting as microtubule organizing centers; pericentrosomal material maturation in activated microglia is inhibited by microtubule stabilization (Taxol). This graphical abstract was created using BioRender.com.

Summary

Microglia are the resident immune cells of the brain, crucial for the maintenance of the homeostasis in the central nervous system. They are responsible for removing cellular debris, pathogens, and damaged cells, as well as modulating neuronal function. Microglia actively and continuously patrol their local environment by using highly motile processes and ramified morphology. In response to triggering stimuli, such as infection, altered neuronal activity, trauma or neurodegenerative diseases, microglia undergo a process of activation that profoundly change their gene expression and functions. Microglia activation is a salient feature of neuroinflammation, prominent in many neurodegenerative diseases. Interestingly, microglia reactivity also entails a large-scale remodeling of cellular geometry, but while the role of the actin cytoskeleton in driving these morphological changes and the specialized functions of activated microglia has been extensively studied, the behavior of the microtubule cytoskeleton during these changes remains unexplored. Microtubules are hollow, cylindrical polymers composed of protofilaments of α/β tubulin heterodimers that arrange in a head-to-tail fashion, making microtubule polarized structures with a fast growing plus end and a slow growing minus end. Microtubules form the backbone of the cell's internal transport system for macromolecules and organelles and are also involved in cell division and the maintenance of cell shape and integrity.

We hypothesize that rearrangement of the microtubule cytoskeleton would play a major role in the morphological changes guiding microglia transition from homeostatic to activated states providing a novel target to modulate microglia activation.

Through a detailed *in vitro* phenotyping approach and validation in mouse retinal tissue we report that: 1) in homeostatic conditions, ramified microglia possess stable microtubule arrays, while microglia activation increases microtubule dynamic behavior. 2) A non-centrosomal microtubule organization in arrays with mixed polarity is a hallmark of homeostatic microglia, similar to the architecture typical of highly specialized cells such as neurons and oligodendrocytes, while activation induces recruitment of the majority of microtubule minus end at the centrosome. 3) Homeostatic

microglia nucleate non-centrosomal microtubules at Golgi outposts, similar to what occurs in neurons, while activating signaling induces recruitment of nucleating material nearby the centrosome, a process inhibited by microtubule stabilization.

Our results unveil the remodeling of the microtubule cytoskeleton as a striking hallmark of microglia reactivity and suggest that while pericentrosomal microtubule nucleation may serve as a distinct marker of activated microglia, inhibition of microtubule dynamics may provide a novel strategy to reduce microglia reactivity in inflammatory disease.

Introduction

Microglia origin and role during neurodevelopment

Microglia are the primary resident immune cells of the brain, which act like active surveillant of the surrounding environment and as the principal central nervous system (CNS) phagocytes.

Pio del Rio-Hortega introduced the concept of microglia in 1919 as a "third element" in the CNS, neurons representing the "first element" and astrocytes and oligodendrocytes being the "second element" (Pérez-Cerdá *et al.* 2015, Sierra *et al.* 2019), foreseeing the distinctiveness of these cells. Although being debated for years, there is now a general consensus on microglia representing an ontogenically distinct population: differently from neurons, oligodendrocytes and astrocytes, deriving from the neuroectoderm, microglia have a mesodermal origin and then migrate into the CNS during neurodevelopment. In mice, microglia arise from primitive myeloid progenitors from the yolk sac before embryonic day 8 and invade the embryo by embryonic day 10.5 (Ginhoux *et al.* 2010). In humans, microglial precursors invade the brain primordium around 4.5 to 5.5 gestational weeks (Andjelkovic *et al.* 1998). Their myeloid lineage is therefore distinct from that of peripheral macrophages that originate from hematopoietic stem cells and maturate in bone marrow.

While migrating, microglia display an amoeboid morphology and acquire a ramified phenotype only after invading the brain parenchyma, where they expand within six post-natal weeks (Kim *et al.* 2015, Nikodemova *et al.* 2015).

During the first 2 weeks of postnatal development, microglia contribute to shaping and establishing appropriate synaptic connections in a process termed "synaptic pruning" where, through phagocytosis of dendritic spines, a subset of synapses are maintained and strengthened, while immature synapses are eliminated, on the basis of functional activity patterns (Hua and Smith 2004, Paolicelli *et al.* 2014).

Once established, microglia density is maintained throughout the entire life with a slow turnover, being long-lived cells (Eyo and Wu 2019) capable of self-renewal, enabling them to repopulate the

brain after depletion without any contribution from bone-marrow derived cells (Ajami *et al.* 2007). Each microglia cell acquires a distinct, nonoverlapping territory of competence that will be then steadily maintained.

Microglia can be identified with several markers, typically: transcription factors such as Pu.1, cytoplasmic markers such as ionized calcium-binding adapter molecule 1 (IBA1), and surface markers as purinergic receptor P2YR12, transmembrane protein 119 (TMEM119), and colony stimulating factor receptor (CSF1R), a key signaling pathway in microglial development (Paolicelli *et al.* 2022).

Microglia function in homeostatic conditions

For a long time microglia have been considered to be resting cells, depicted as inactive sentinels prone to respond in case of injury. Live imaging of the healthy brain has then demonstrated that microglia are highly dynamic patrolling cells (Davalos *et al.* 2005, Nimmerjahn *et al.* 2005, Raivich 2005), having a unique cluster of transcripts encoding proteins for sensing endogenous ligands and microbes, defined as "sensome" (Hickman *et al.* 2013). The advent of new genetic and imaging tools has led to the discovery of an increasing number of microglia physiological functions.

In the adult brain, microglia are present in the subventricular zone and subgranular zone of the dentate gyrus, neurogenetic niches that produce neurons that integrate into the olfactory bulb and hippocampus. Here ramified, unchallenged microglia phagocyte apoptotic newborn neurons (Tremblay *et al.* 2011, Eyo and Wu 2019), differently from phagocytic microglia cells in neurodegeneration, which are typically amoeboid (Kettenmann 2007).

In their homeostatic state, microglia exhibit a ramified morphology characterized by small non motile cell somata and long branched processes that terminate with bulbous endings. Microglia processes continuously extend and retract (Nimmerjahn *et al.* 2005, Bolasco *et al.* 2018), clearing cellular debris, remodeling and eliminating synapses, actively remodeling the perisynaptic environment, and releasing soluble factors (Tremblay *et al.* 2010, Paolicelli *et al.* 2011, Parkhurst *et al.* 2013, Colonna and Butovsky

2017, Basilico *et al.* 2019, 2021, Bernier *et al.* 2019). In addition, through engagement of purinergic and glutamate receptors, microglia processes can extend and wrap around swollen axons to prevent excitotoxicity (Colonna and Butovsky 2017).

Microglia can communicate with neighboring cells by cell-to-cell contact or by release of soluble factors and biomolecules through secreted vesicles, as exosomes and microvesicles (MVs). MVs are extracellular vesicles with size ranging from 100 nm to 1 μm that originate by direct budding of plasma membrane into the extracellular space, selectively packaging cellular components to be released (Turola *et al.* 2012, Paolicelli *et al.* 2019).

Microglial heterogeneity: states and shapes in pathological conditions

Microglia are the tissue-resident macrophages of the CNS and represent the first line of defense against any threats to the brain homeostasis. In response to invading pathogens, endogenous misfolded proteins, malignant cells, tissue injury or in neurodegenerative disorders, microglia undergo a varied and context-dependent process of activation, acquiring different interchangeable phenotypes depending on the stimuli (Hanisch 2002, Kettenmann *et al.* 2011, Colonna and Butovsky 2017, Madry *et al.* 2018).

Although reductively, microglia activation is often categorized as either classical or alternative, following the classification used for macrophages (Durafourt *et al.* 2012, Cherry *et al.* 2014). The classical activation is typically induced by stimulation of Toll-like receptors (TLRs), for example trough lipopolysaccharides (LPS), and IFN-γ signaling pathways. Being the primary immune cells of the brain, microglia are major players in neuroinflammation, releasing inflammatory mediators as cytokines, reactive oxygen species and soluble lipids (Graeber *et al.* 2011). Classically activated microglia typically produce proinflammatory cytokines and chemokines, such as TNF-α, IL-6, IL-1β as well as inducible nitric oxide synthase (iNOS), and the release of microvesicles is significantly increased (Paolicelli *et al.* 2019). In this activated state, reactive microglia exhibit phagocytic activities and,

if over-activated, they are thought to contribute to brain damage and neurodegeneration (Heneka *et al.* 2014, Colonna and Butovsky 2017). On the other hand, alternative activation typically triggers the anti-inflammatory and repairing activities of microglia. It can be induced by IL-4, IL-13, IL-10 and promotes the release of anti-inflammatory cytokines, such as IL-10 and TGF-β, induces arginase 1 and is characterized by the secretion of growth and neurotrophic factors (Colonna and Butovsky 2017).

When cell bodies enlarge and cell processes shorten, microglia morphology is usually described as amoeboid, and usually this reflects a highly activated state associated with pro-inflammatory function. In addition to amoeboid forms, bipolar rod-shaped microglia that form strings of cells aligned end-to-end at the damaged site have also been observed after brain injury (Tam and Ma 2014). Thus, the cell shape and morphology is often taken as a hint of microglia activation, reflecting their responses to a broad variety of stimuli.

The microtubule cytoskeleton

Microtubules (MTs) are prominent elements of the cytoskeleton that represent a track for the intracellular transport and a scaffold for organelle positioning. Cell shape, mechanics, proliferation and movement rely on the organization of the microtubule network.

MTs are hollow, cylindrical polymers composed of thirteen protofilaments of α/β tubulin heterodimers arranged in a head-to-tail fashion (Nogales *et al.* 1999). Head-to-tail association of tubulin dimers makes microtubule polarized structures, characterized by a fast growing plus end and a slow growing minus end. The minus ends are often stabilized and anchored at specific cellular sites (Akhmanova and Steinmetz 2019). On the other hand, usually the polymerizing plus end is bound by end binding (EB) proteins (Bieling *et al.* 2008, Mustyatsa *et al.* 2019). In neurons, MT polarity is important to define the direction of the transport, since motor proteins recognize MT polarity and drive transport to either the minus

end (dynein) or plus end (kinesins) (Klinman and Holzbaur, 2018; Reck-Peterson *et al.*, 2018).

MTs are generally highly dynamic structures constantly undergoing stochastic transitions from polymerization to depolymerization (catastrophe events) and vice-versa (rescue events), in a process termed dynamic instability, with the two dynamic states exhibiting characteristic rates of growth or shrinkage (Mitchison and Kirschner 1984). The dynamics of MTs is determined mainly by the rate of guanosine triphosphate (GTP) hydrolysis. Both α-tubulin and β-tubulin bind GTP, but only the GTP bound to β-tubulin is hydrolyzed after the α/β heterodimer is incorporated into the microtubule lattice. As a result, a cap of GTP-tubulin is present at the plus ends, maintaining the microtubule in a growth state (Waites *et al.* 2021, Akhmanova and Kapitein 2022). MT dynamic properties can be modulated by tubulin post-translational modifications (PTMs): PTMs preferentially accumulate on stable MTs, since stabilized MTs resist disassembly and live long enough to become substrates of tubulin modifying enzymes that add molecular moieties on either the α- or β-tubulin subunit. The combinatorial nature of these modifications provides a "tubulin code" which controls a variety of functions, including organelle transport and the mechanical properties of the MT lattice (Janke and Bulinski, 2011; Gadadhar *et al.*, 2017; Janke and Magiera, 2020).

MT orientation, density, and post-translational modifications all respond and contribute to breaking cellular symmetry (Etienne-Manneville 2013, Meiring and Akhmanova 2020). Cell polarity depends on the asymmetric distribution of organelles, proteins and cellular structures. In eukaryotes, changes in cellular symmetry are associated with massive reorganization of both the actin and microtubule cytoskeletons: indeed, the presence of an intrinsically polar object is what causes the breakage of the symmetry. While actin and actin-based motor proteins are required for breaking the symmetry in most cells, specification of polarity in neurons depends on MTs and MT associated proteins (Li and Gundersen 2008). In migrating or dividing animal cells, the main MTOC is represented by the centrosome, a spherical structure composed by a mother and a daughter centriole surrounded by a matrix of pericentriolar material (PCM), that contains proteins important for cell cycle regulation,

nucleation of MTs, stabilization and attachment of MT minus ends (Conduit *et al.* 2015, Rev *et al.* 2017). In these cells, the arrays are radial; the MT plus end is located distal to the centrosome and the minus end is at or near the centrosome. Establishment of cell polarity can be achieved through centrosome repositioning or by the formation of non-radial MT arrays, in which MTs are not preferentially nucleated at the centrosome (Vinogradova *et al.* 2009, Akhmanova and Hoogenraad 2015, Alieva *et al.* 2015). During this transition, the centrosome typically loses its maximal MT nucleating activity, while self-organizing assemblies of MT nucleating material distant from the centrosome, or sites of acentrosomal nucleation as the Golgi complex, the nuclear envelope, the plasma membrane, intracellular membranes, serve as non-centrosomal MTOCs. This transition is typical of neurodevelopment.

MT nucleation at the Golgi is important in neurons, where long branches require sites of MT nucleation provided by satellite acentrosomal MTOCs termed Golgi outposts, sometimes also referred to as "Golgi vesicles", "satellite Golgi", "mini Golgi", or "Golgi elements" (Kassandra M. Ori-McKenney *et al.* 2012, Lewis and Polleux 2012, Valenzuela *et al.* 2020). The Golgi outpost is an organelle that shares common markers with the perinuclear Golgi body, such as cis-Golgi matrix protein 130 (GM130), but is typically much smaller in size (1–2 μm in diameter or length) and located far from the nucleus or cell body. The presence of this nucleating organelle has been also recently characterized in oligodendrocytes (Fu *et al.* 2019). When cells are characterized by a non-centrosomal array, typically the released free MT minus-end are capped and stabilized by members of the calmodulin-regulated spectrin-associated protein (CAMSAP) family (Bartolini and Gundersen 2006, Akhmanova and Steinmetz 2019).

Microtubules in microglia

So far, few studies characterized microglia MT cytoskeleton. In basal *in vivo* conditions, microglia display major processes (~ 2 μm in diameter) that contain microtubules forming a stable cellular backbone, while minor processes (<0.5 μm in diameter) contain actin-rich filopodia. Minor processes are more dynamic (Bernier *et*

al. 2019) than major processes, which have been shown to colocalize with acetylated and detyrosinated tubulin (Ilschner and Brandt 1996), two PTMs that accumulates on stable MTs, indicating that microglia major processes may contain stabilized microtubules. Indeed, the work of Ilschner and Brandt from 1996 showed that while in amoeboid cells the modified microtubules were restricted to regions close to the MTOCs, long and continuous stretches of microtubules were positive for acetylated tubulin in the cell body and the processes of ramified cells, with no apparent anchoring at MTOCs. The increase in acetylated and detyrosinated microtubules was also paralleled by an increased stability against nocodazole-induced microtubule disassembly and by a lower rate of change in the length of the processes (Ilschner and Brandt 1996).

Recently, it was disclosed a role for the centrosome in regulating the rate of efficient removal of apoptotic neuronal cells by microglia *in vivo* (Möller *et al.* 2022). During this process, termed efferocytosis, microglia generate multiple microtubule-based branches, but they only successfully engulf one apoptotic neuron at a time with a sequential pattern, and targeted movement of the microglial centrosome into branches predicts successful neuronal engulfment.

Aim of the project

The heterogeneous and complex process of microglia activation is characterized by massive morphological changes, with microglia cells - typically ramified in homeostatic conditions - acquiring an amoeboid structure in presence of activating stimuli. Throughout neuronal differentiation, the microtubule cytoskeleton reorganization to a non-centrosomal array drives the acquisition of a polarized structure: during this transition, microtubule orientation, density, and post-translational modifications are key determinants in breaking cellular symmetry and establishing cell polarity.

Early studies suggested changes in microtubule spatial organization and stability with microglia activation (Ilschner and Brandt, 1996). Despite these observations, however, only remodeling of the actin cytoskeleton has been extensively studied in microglia (Granucci *et al.* 2003, Uhlemann *et al.* 2016, Bernier *et al.* 2019, Reichert and Rotshenker 2019, Das *et al.* 2020), while the role of the microtubule cytoskeleton in breaking cellular polarity during the transition from homeostatic to a reactive state has not been explored.

Here we hypothesize that rearrangement of the microtubule cytoskeleton might be required for the morphological changes that guide microglia transition from homeostatic to activated states, and propose the microglia microtubule cytoskeleton rearrangement as a marker for microglia activation, aiming to disclose new therapeutical targets in neuroinflammation.

Results

Homeostatic, activated and alternatively activated primary microglia differ in MT distribution, stability and dynamicity

To investigate the organization of the MT cytoskeleton in homeostatic and reactive microglia, we used primary mouse microglia cultures in which the presence of ramified cells was maintained by growth factors secreted by astrocytes (Bohlen *et al.* 2017). With this approach we prepared a nearly pure population of primary microglia comprised by 99% of Iba1 positive cells with minimal activation. To polarize microglia towards an activated or an alternatively activated state, cells were challenged with either LPS-IFNγ (100 ng/ml – 20 ng/ml, 48 h, defined as "activated") or IL-4 (20 ng/ml, 48 h, defined as "alternatively activated"), and we measured the expression of their signature activation genes (Figure 1A). As revealed by Iba1 staining (Figure 1B), polarized microglia underwent dramatic morphological changes. We classified cell morphology as ramified (≥3 ramifications), ameboid or bipolar based on number of cellular processes, cell area, and solidity, a measure of cell shape complexity (Figure 1B-D). Analysis of morphology distribution under homeostatic, activated and alternatively activated conditions revealed that ramified cells were enriched in untreated microglia (35 ± 3%) (Figure 1B and 1D), while ameboid cells represented a large majority after activating stimulation (82 ± 3%) (Figure 1B and 1D). Conversely, when cells were challenged with an alternatively activating stimulus, microglia mostly acquired a unipolar or bipolar rod-shape morphology (54 ± 3%) characterized by the presence of a lamellipodium and a uropod (Figure 1B and 1D). To investigate in detail the structural changes associated with reactive microglia states in single cells, we chose to select for comparison the most representative morphology of each *in vitro* phenotype: ramified for homeostatic, amoeboid for activated and bipolar for alternatively activated microglia.
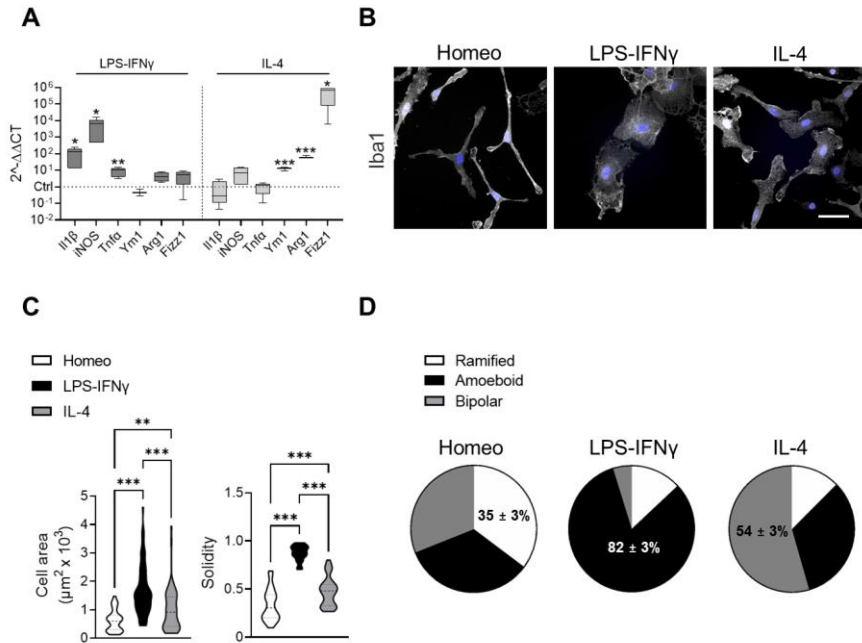
Fig. 1. Molecular and morphological characterization of homeostatic, activated and alternatively activated primary microglia. (**A**) RT-qPCR reveals increased expression of pro-inflammatory (Il1b, iNOS, Tnfα) and anti-inflammatory genes (Ym1, Arg1, Fizz1) upon LPS-IFNγ or IL-4 challenge, respectively. Gene expression is normalized to the housekeeping gene Gapdh, n = 4 independent cultures. Box plots indicate the median, 25th, and 75th percentiles; whiskers show the minimum and maximum. *** p <0.001; ** p <0.01; *p <0.05, Student's t-test. (**B**) Representative images showing Iba1 immunostaining (gray) of microglia in homeostatic (Homeo) condition and following LPS-IFNγ or IL4 treatment (Scale bar: 20 μm. Hoechst for nuclei visualization, blue). (**C**) Violin plots showing cell surface area (left) and solidity coefficient (right) related to Homeo (white), LPS-IFNγ (black) or IL-4 (gray) challenged cells (n = 70 cells for each condition, from 3 independent experiments. *** p <0.001; **p <0.01. Kruskall-Wallis - Dunn's multiple comparisons test for cell area, left; One-way ANOVA - Tukey's multiple comparison test for solidity, right). (**D**) Pie charts illustrating the distribution of cell morphology in Homeo, LPS-IFNγ and IL-4 conditions. Ramified cells are enriched in Homeo (35 ± 3%); amoeboid cells in

LPS-IFNγ (82 ± 3%) treated microglia; bipolar cells in IL-4 (54 ± 3%) treated microglia, n = 3 independent experiments.

We then employed scanning electron microscopy (SEM) and confocal microscopy to identify ultrastructural elements typical of each state (Figure 2A). Homeostatic microglia exhibited many branched processes extending outward from the cell body and multiple filopodia-like structures (Figure 2A) that were also positive for phalloidin staining (Figure 2D). Upon activating challenge, microglia retracted most of their processes and acquired a flattened and round morphology (Figure 2A and 2D). SEM imaging further revealed that activated microglia displayed numerous tethered extracellular vesicles (EVs) blebbing from the cell surface (Figure 2B). Analysis of EV diameter showed a distribution of size ranging from 250 to 650 nm (Figure 2C), consistent with microglia-shedding microvesicles (0.1–1 μm). Notably, these are vesicles represent a typical secretory pathway for the inflammatory cytokine IL-β (Turola *et al.* 2012, Herr *et al.* 2020). Alternatively activated microglia were characterized by extensive membrane ruffling at both uropod and leading edge, which appeared as sheet-like structures on the dorsal cell surface (Figure 2A and 2D).
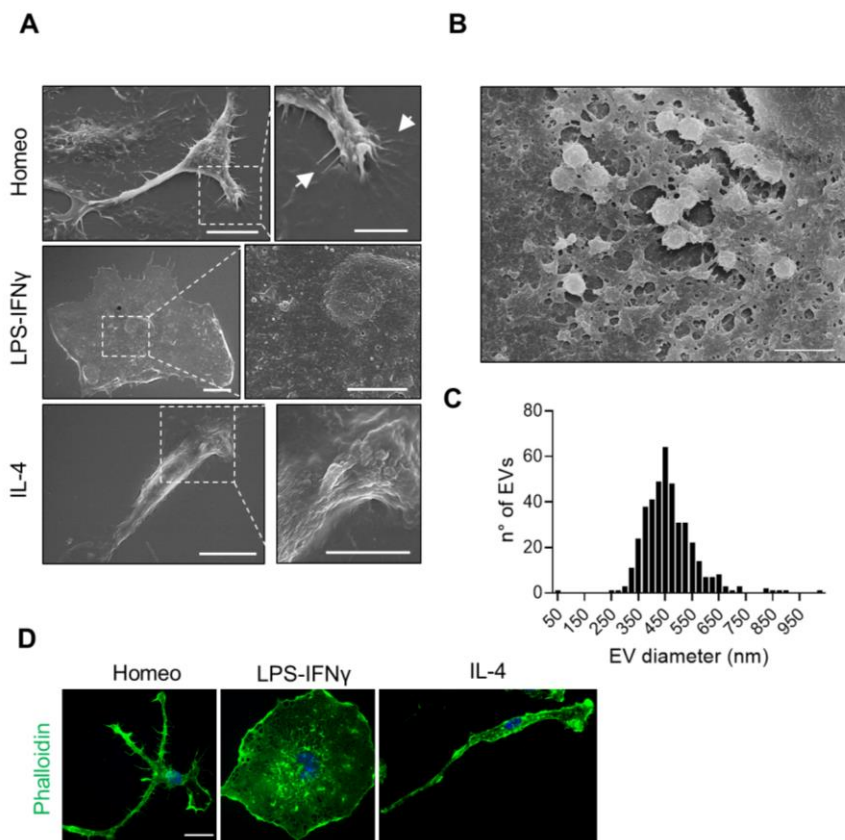
Fig. 2. Homeostatic, activated and alternatively activated primary microglia display different anatomical structures. (A) Representative scanning electron micrographs of microglia in homeostatic (Homeo, top), LPS-IFNγ (middle) and IL-4 (bottom) conditions. Ramified cells (Homeo) show filopodia extensions as indicated by arrows, ameboid cells (LPS-IFNγ) exhibit numerous extracellular vesicles (EVs) on the cell surface, while bipolar cells (IL-4) are characterized by extensive membrane ruffling on the cell surface and leading edge. Scale bar: 10 μm; zoom, 5 μm. **(B)** Scanning electron micrographs showing EVs on the LPS-IFNγ cell surface at higher magnification. Scale bar: 2 μm. **(C)** Distribution of EV size measured on the ameboid cell surface. n = 22 cells. **(D)** Representative confocal images of microglia labelled with Alexa Fluor 488-conjugated phalloidin (green). Ramified cells (Homeo) exhibit filopodia like structures (as indicated by arrows) while ameboid (LPS-IFNγ) and bipolar cells (IL-4) are characterized by

membrane ruffles along cell borders and at lamellipodia (as indicated by arrows). Scale bar: 25 μm. Hoechst for nuclei visualization, blue.

We began to analyze the MT cytoskeleton in each functional state by immunofluorescence (IF) staining of tyrosinated α-tubulin (Tyr tub), a bulk tubulin marker labeling the entire MT network. To do this, we designed an original code to compute the profile plot of the maximum intensity pixel as a function of distance from a center in the cell (Figure 3A). In this way, we obtained an analysis tool useful to describe the distribution of a protein inside the cell that is independent of cell shape. MTs appeared to be packed in the cellular branches extending from the cell body in both homeostatic and alternatively activated microglia (Figure 3B), while MTs distributed radially from a perinuclear region in activated microglia (Fig. 3B). Radial profiling of Tyr tub intensity (Figure 3C), confirmed that MT staining was uniformly distributed along the cell profile in homeostatic and alternatively activated microglia, while in activated cells, Tyr tub signal rapidly decayed at increasing distances from a perinuclear region (Figure 3C; exponential decay constant $k_{LPS-IFN\gamma} = 0.046 \pm 0.001$; $k_{homeo} = 0.013 \pm 0.002$; $k_{IL-4} = 0.015 \pm 0.002$).
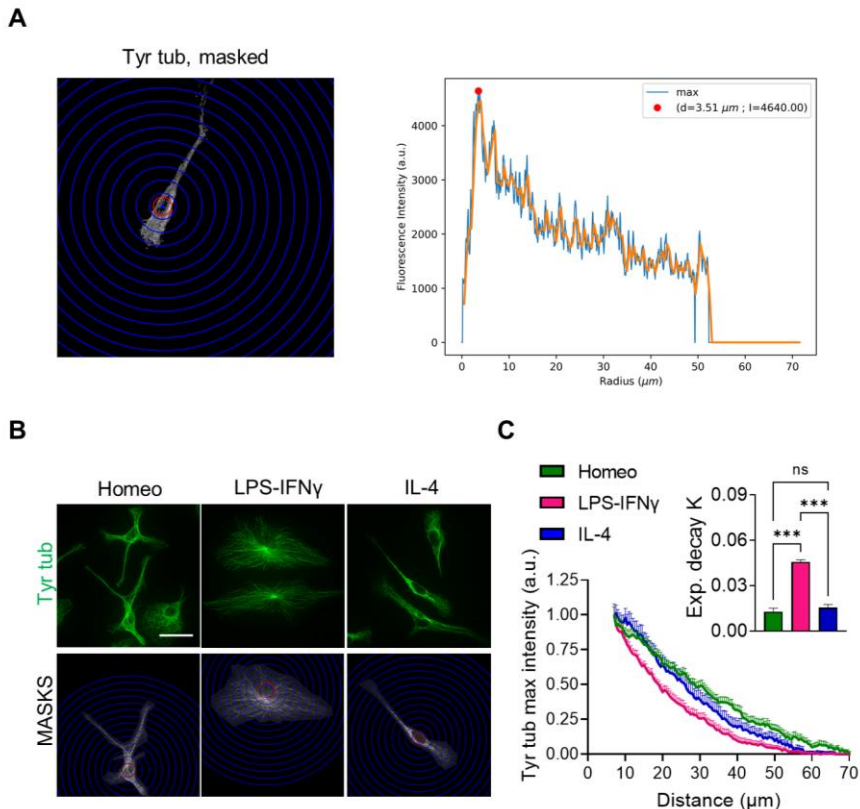
Fig. 3. Homeostatic, activated and alternatively activated primary microglia differ in MT distribution. (A) Example of the analysis products obtained with max Intensity RadialProfile script in Python language. *Left*, representative immunofluorescence image of tyrosinated α-tubulin (Tyr tub, white) staining, where a mask is applied to isolate the cell. The concentric blue circles overlaying the image are used to compute the profile plot of the maximum intensity pixel (*right*) as a function of distance from a center in the image. Red circle indicates the radius corresponding to the largest intensity value. **(B)** Representative immunofluorescence images of Tyr tub (green) staining in homeostatic (Homeo), activated (LPS-IFNγ) and alternatively activated (IL-4) microglia (*top*; scale bar: 20 µm) and corresponding masks (MASKS) used for the analysis (*bottom*), with radial scale (unit = 5 µm; blue circles) centered at the centroid of the cell nucleus. **(C)** Plot showing maximum fluorescence intensity values of Tyr tub vs the radial distance from cell nucleus, obtained with radial profiling, in Homeo (n = 38, green),

LPS-IFNγ (n = 31, magenta) or IL-4 (n = 38, blue) treated microglia. Curve fit was performed using a single exponential decay function. *Insert:* bar chart reporting the exponential decay constant values (K) for each condition (values are expressed as mean ± SEM from 4 independent experiments; *** p <0.001, One-way ANOVA – Tukey's multiple comparison test). Note faster decay of Tyr tub signal in Activated microglia.

To evaluate whether MTs differed in stability according to the reactive state, we analyzed levels and distribution of detyrosinated and acetylated tubulins, two independent tubulin post-translational modifications (PTMs) associated with MT longevity (Webster and Borisy 1989, Janke and Magiera 2020). Semiquantitative IF analyses revealed that homeostatic cells had the highest level of both detyrosinated (Figure 4B, left) and acetylated (Figure 4B, right) tubulin compared to activated or alternatively activated microglia (De-tyr/Tyr tub: 0.30 ± 0.03; 0.04 ± 0.01; 0.03 ± 0.01, Acetyl/Tyr tub: 1.02 ± 0.05; 0.69 ± 0.04; 0.72 ± 0.04 in homeostatic, activated and alternatively activated microglia respectively; Figure 4B), suggesting that homeostatic microglia display more stable MTs.
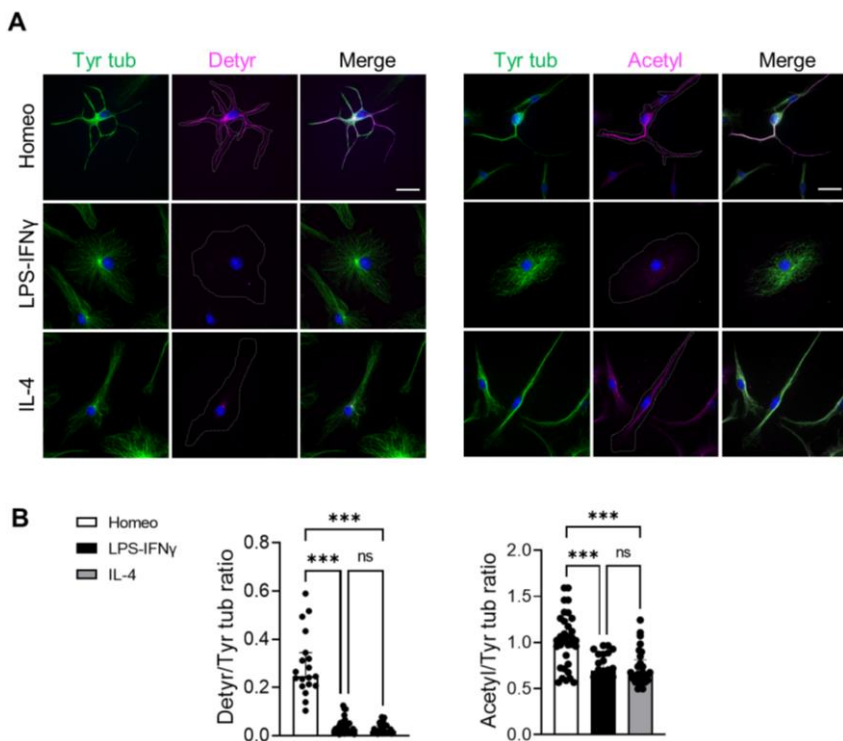
Fig. 4. Homeostatic, activated and alternatively activated primary microglia show different distribution of MT post-translational modifications. (A) Representative IF images of Homeo, LPS-IFNγ or IL-4 treated microglia: *left*, co-staining of Tyr tub (green) and de-tyrosinated tubulin (Detyr, magenta) (scale bar: 20 µm. Hoechst for nuclei visualization, blue); *right*, co-staining of Tyr tub (green) and acetylated tubulin (Acetyl, magenta) (scale bar: 20 µm. Hoechst for nuclei visualization, blue). **(B)** Scatter dot plots showing IF signal quantification of detyrosinated/ tyrosinated (Detyr/Tyr) tub ratio (*left*, Homeo n = 19, LPS-IFNγ n = 32, IL-4 n = 28 cells from 3 independent experiments) and acetylated/tyrosinated (Acetyl/Tyr) tubulin ratio (*right*; Homeo n = 33, LPS-IFNγ n = 25, IL-4 n = 29 cells from 3 independent experiments). Values are expressed as median ± interquartile range; *** p <0.001; Kruskall-Wallis - Dunn's multiple comparisons test. Note that microglia challenged with LPS-IFNγ or IL-4 have reduced tubulin PTM levels compared to Homeo cells.

We then observed the behavior of MTs labeled with SiR-tubulin, a fluorogenic probe with low cytotoxicity for fluorescence imaging of tubulin in living cells (Lukinavičius *et al.* 2014), focusing

on shallow peripheral sections of the cell to measure MT dynamics using time lapse wide field fluorescence microcopy (Figure 5A). No change was observed among the three different microglia states in rescue frequency (frequency of transitions from shrinkage to growth) or the fraction of time spent in pausing or shrinkage. However, while in activated and alternatively activated microglia MTs exhibited a moderate yet significative drop in catastrophe frequency (frequency of transitions from growth to shrinkage), they also significantly enhanced their growth rates and acquired a nearly 2.5 fold increase in rates of shrinkage, resulting in an overall net rise in MT dynamicity compared to MTs of homeostatic cells (0.06 ± 0.01; 0.08 ± 0.01; 0.09 ± 0.01 in homeostatic, activated and alternatively activated microglia respectively; Figure 5B and 5C).

A SirTub

B

Legend:
- ☐ Homeo
- ■ LPS-IFNγ
- ▨ IL-4

C

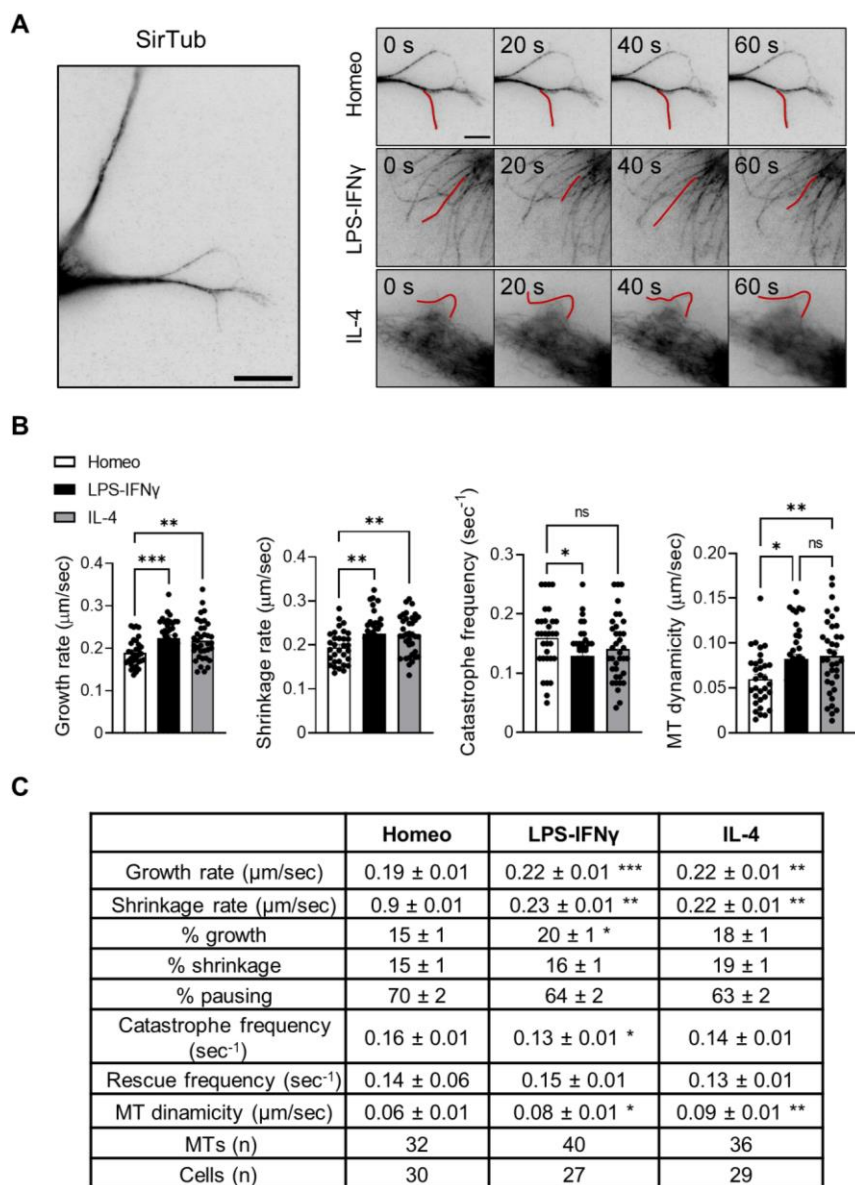|	Homeo	LPS-IFNγ	IL-4
Growth rate (µm/sec)	0.19 ± 0.01	0.22 ± 0.01 ***	0.22 ± 0.01 **
Shrinkage rate (µm/sec)	0.9 ± 0.01	0.23 ± 0.01 **	0.22 ± 0.01 **
% growth	15 ± 1	20 ± 1 *	18 ± 1
% shrinkage	15 ± 1	16 ± 1	19 ± 1
% pausing	70 ± 2	64 ± 2	63 ± 2
Catastrophe frequency (sec⁻¹)	0.16 ± 0.01	0.13 ± 0.01 *	0.14 ± 0.01
Rescue frequency (sec⁻¹)	0.14 ± 0.06	0.15 ± 0.01	0.13 ± 0.01
MT dinamicity (µm/sec)	0.06 ± 0.01	0.08 ± 0.01 *	0.09 ± 0.01 **
MTs (n)	32	40	36
Cells (n)	30	27	29

Fig. 5. Homeostatic, activated and alternatively activated primary microglia differ in dynamic behavior. (A) *Left*, Representative inverted contrast widefield frame from time lapse acquisitions showing SiR-Tubulin labeling. Scale bar 20 µm. *Right,* representative inverted contrast widefield frames from time lapse

acquisitions of SiRtubulin in homeostatic (Homeo), LPS-IFNγ or IL-4 treated microglia at 4 different timepoints (0 s, 20 s, 40 s, 60 s). Red lines highlight MT length changes ≥0.5 μm between frames. Scale bar: 5 μm. **(B)** Scatter dot plots representing (from *left* to *right*) growth rate, shrinkage rate, catastrophe frequency and MT dynamicity in Homeo, LPS-IFNγ and IL-4 microglia. Values are expressed as mean ± SEM (Homeo n = 30, LPS-IFNγ n = 27 and IL-4 n = 29 cells from 4 independent experiments). *** p <0.001; ** p <0.01; * p <0.05. One-way ANOVA - Dunnett's multiple comparison test. **(C)** Table reporting parameters of MT dynamics obtained from wide field fluorescence time lapse analysis of SiRTubulin in homeostatic (Homeo), activated (LPS-INFγ) and alternatively activated (IL-4) microglia. Values are expressed as mean ± SEM from Homeo n = 32/30 MTs/cells, LPS-INFγ n = 40/27 MTs/cells and IL-4 n = 36/29 MTs/cells arising from 4 independent experiments. *** p < 0.001; ** p < 0.01; * p < 0.05. One-way ANOVA - Dunnett's multiple comparison test.

In summary, and consistent with our analysis of tubulin PTMs, these data suggest that microglia acquisition of activated and alternatively activated phenotypes is characterized by loss of MT stability and an increase in MT dynamics.

Homeostatic, activated and alternatively activated microglia differ in MT orientation

In most dividing and motile cells, the centrosome is responsible for MT nucleation and anchoring, leading to the formation of radial MT arrays in which all MT minus ends are attached to the centrosome, while MT plus ends extend towards the cell periphery. In contrast, in most differentiated, stationary and axially polarized cells, MTs are more stable and organized in non-centrosomal arrays that are non-radially anchored at the centrosome (Bartolini and Gundersen 2006).

We hypothesize that microglia activation would be paralleled by prominent changes in cell polarity driven by the remodeling of MT anchoring and orientation. To test this, we analyzed the localization and expression of MT plus end and minus end (EB and CAMSAP, respectively) markers in homeostatic, activated and alternatively activated microglia cells. While EBs are widely adopted markers of actively growing MT plus ends (comets), since they bind to the GTP cap, members of the CAMSAP family regulate the

formation and stability of non-centrosomal MT arrays by capping free MT minus ends (Yau *et al.* 2014, Akhmanova and Hoogenraad 2015).

Lentiviral expression of EB3-EGFP showed 13% (n=13 cells) of retrograde EB3 comets in homeostatic ramified microglia and 12% (n=6 cells) in alternatively activated bipolar microglia, suggesting the existence of bioriented arrays (Figure 6A, and 6B). We had no success in infecting LPS-IFNγ microglia. In addition, in infected homeostatic microglia, we found increased values of cell area (1123 ± 111 cm^2) and solidity (0.39 ± 0.03) compared to non-infected cells (see Figure 1C), indicating that viral infection my impact on microglia reactivity state. To identify MT polarity in non-infected cells, we thus took advantage of the comet-shaped accumulation of EBs at MT ends, with comet tail intensity decaying exponentially after the maximum at the MT end (Bieling *et al.* 2008). First, we measured fluorescence intensity gradients of EB comets from single frames of our movies (Figure 6A and 6B, arrows) and confirmed that this approach was reliable to identify comet orientation. Next, we applied this analysis to microglia cells that had been fixed and immunostained using EB1 and tyrosinated tubulin antibodies (Figure 6C).
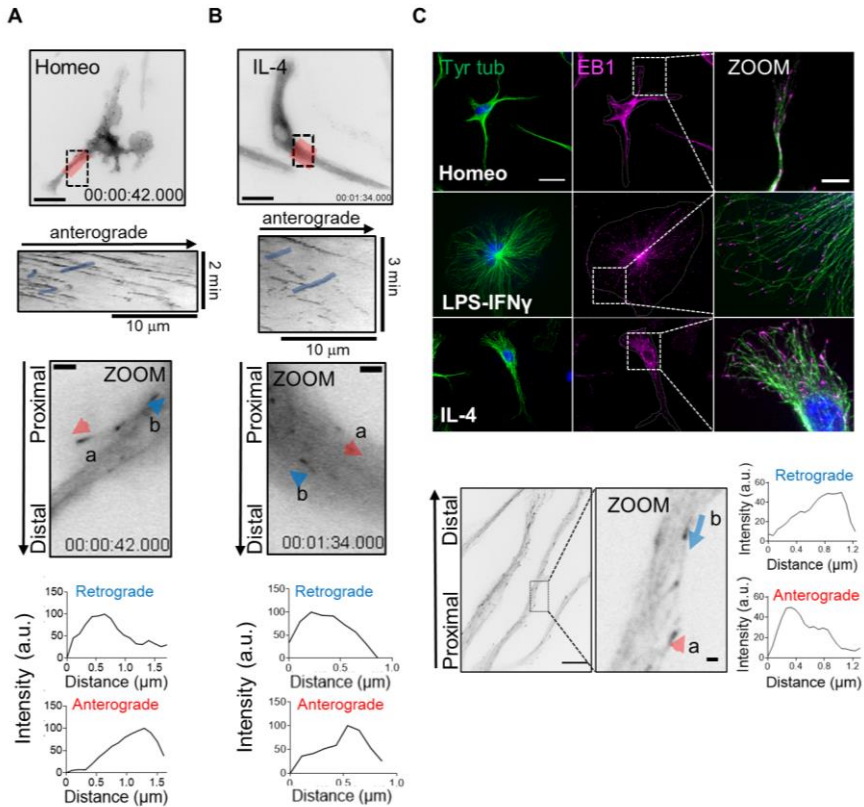
Fig. 6. Homeostatic, activated and alternatively activated primary microglia differ in MT plus end orientation. (A) *Top,* representative inverted contrast widefield frames from time lapse acquisitions of EB3-EGFP infected homeostatic (Homeo) microglia (scale bar: 20 μm) and kymograph of the selected region in red (*middle*). Note that retrograde comets in the kymograph are highlighted in blue. *Bottom*, inverted contrast single frame image of EB3-EGFP at higher magnification (scale bar: 2 μm). Relative orientation of EB3 comet peaks with respect to the cell nucleus was used to distinguish between EB3 anterograde (a, red arrow) and retrograde (b, blue arrow) comets. **(B)** *Top*, representative inverted contrast widefield frame from time lapse acquisitions of EB3-EGFP infected alternatively activated (IL-4) microglia (scale bar: 20 μm) and kymograph of the selected region in red (middle). Note that retrograde comets in the kymograph are highlighted in blue. *Middle*, inverted contrast single frame image of EB3-EGFP at higher magnification (scale bar: 2 μm). Relative orientation of EB3 comet peaks with respect to the cell nucleus was used to distinguish between EB3 anterograde (a, red arrow) and retrograde (b, blue arrow) comets. **(C)** *Top,* representative IF images of EB1 (magenta) and tyrosinated α-tubulin (Tyr tub) (green) in homeostatic

(Homeo), activated (LPS-IFNγ) and alternatively activated (IL-4) microglia. Scale bar: 20 μm; zoom: 5 μm. Hoechst for nuclei visualization, blue. *Bottom,* representative inverted contrast single plane image of EB1 IF (*left*. Scale bar 10 μm). Direction of EB1 signal gradient relative to the cell nucleus was used to identify EB1 anterograde (a, red arrow) and retrograde (b, blue arrow) comets (*middle*, scale bar: 2 μm). *Left*: intensity profile of anterograde (*top*) and retrograde (*bottom*) comets.

Confocal immunofluorescence analysis showed that in activated and alternatively activated microglia, EB1 decorated most free MT ends (Tyr tub stained) (activated, 88%; alternatively activated, 82%) that extended towards the cell periphery (Figure 6C), confirming the existence of a prominent pool of dynamic MTs arranged radially with their minus ends attached to a perinuclear region of the cell. EB1 comets were visible at MT ends in homeostatic microglia (homeostatic 63% of MTs $p < 0.001$, Figure 7A), although to a lesser extent. At the same time, western blot analysis of whole cell lysates showed that total EB1 protein levels did not change in reactive microglia compared to homeostatic cells (Figure 7B). Analysis of fluorescence intensity gradients of EB positive comets (Figure 6C, arrows; Figure 7C) confirmed the presence of a pool of retrograde comets in homeostatic microglia and alternatively activated microglia, while activated microglia displayed the majority of the comets outwardly oriented (23.4%, 12.5% and 0.5%, respectively; $p < 0.001$, Figure 7C).
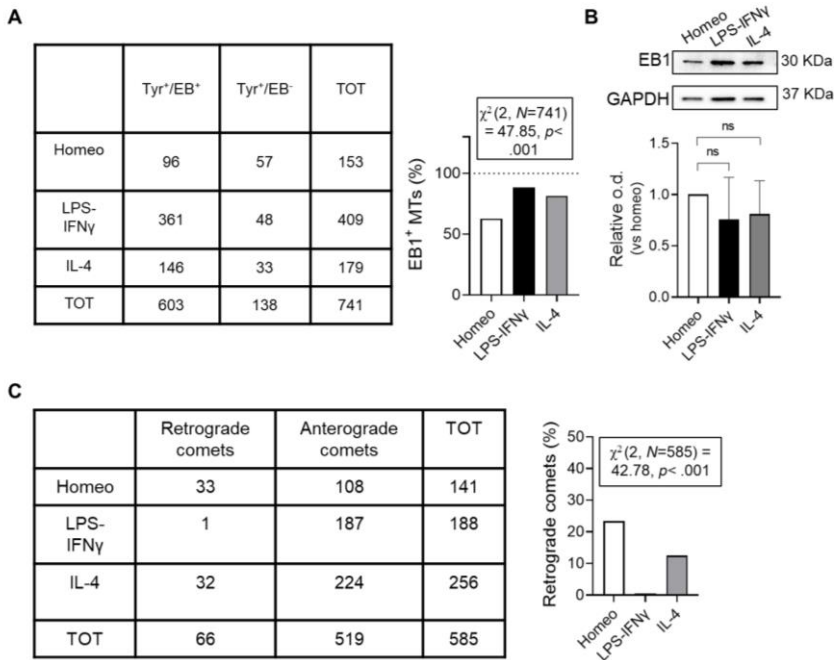
A

	Tyr⁺/EB⁺	Tyr⁺/EB⁻	TOT
Homeo	96	57	153
LPS-IFNγ	361	48	409
IL-4	146	33	179
TOT	603	138	741

$\chi^2(2, N=741) = 47.85, p< .001$

EB1⁺ MTs (%)

B

EB1 — 30 KDa
GAPDH — 37 KDa

Relative o.d. (vs homeo)

ns, ns, p=0.31

C

	Retrograde comets	Anterograde comets	TOT
Homeo	33	108	141
LPS-IFNγ	1	187	188
IL-4	32	224	256
TOT	66	519	585

$\chi^2(2, N=585) = 42.78, p< .001$

Retrograde comets (%)

Fig. 7. Analysis of EB1 expression in homeostatic, activated and alternatively activated microglia. (**A**) Contingency analysis of EB1 and tyrosinated α-tubulin (Tyr) co-staining in homeostatic (Homeo) condition and following LPS-IFNγ or IL4 treatment: number of double positive comets are reported in the bar chart, χ^2 parameters are reported in the insert. (**B**) *Bottom*: bar chart reporting the amount of EB1 protein level in microglia phenotypes; *top*: representative immunoblot of EB1. Values are expressed as median ± interquartile range from 4 independent experiments. p=0.31, Mann Whitney test. (**C**) Contingency analysis of comets in Homeo, LPS-IFNγ or IL-4 challenged microglia: number of retrograde comets are reported in the bar chart, χ^2 parameters are reported in the insert.

Detection of a pool of retrograde comets in homeostatic microglia suggested the presence of non-centrosomal MT arrays, which we investigated by analyzing the expression and distribution of CAMSAP2. Western blot analysis of whole cell lysates revealed higher CAMSAP2 level in homeostatic microglia (Figure 8A). However, while in homeostatic and alternatively activated cells CAMSAP2 often distributed along cell ramifications (Figure 8B and 8C arrows), CAMSAP2 signal was detectable only around the

perinuclear region in activated microglia (Figure 8B and 8C). We used radial profiling of CAMSAP2 fluorescence intensity (Figure 8D) as a measure of CAMSAP2 distribution in the cytosol, and we confirmed that in activated microglia CAMSAP2 signal decayed more rapidly at increasing distances from the perinuclear region than in homeostatic and alternatively activated cells (Figure 8D).
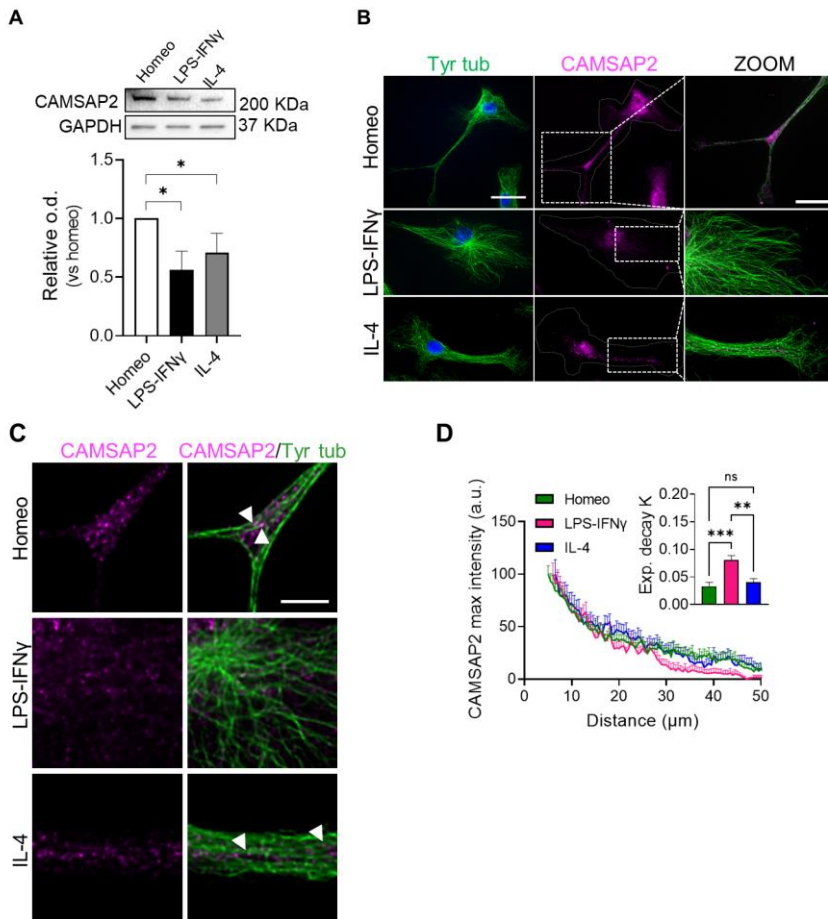

Fig. 8. Homeostatic, activated and alternatively activated primary microglia differ in CAMSAP2 distribution. (A) *Bottom*: bar chart reporting the amount of CAMSAP2 protein level in microglia phenotypes; *top*: representative immunoblot of CAMSAP2. Values are expressed as median ± interquartile range from 4

independent experiments. * p <0.05, Mann Whitney test. **(B)** Representative z-projection confocal images showing CAMSAP2 (magenta) and tyrosinated α-tubulin (Tyr tub, green) signal in homeostatic (Homeo), LPS-IFNγ or IL-4 treated microglia. Scale bar: 20 μm; zoom: 5 μm. Hoechst for nuclei visualization, blue. **(C)** Single confocal planes at higher magnification of CAMSAP2 (magenta) and Tyr tub (Green) signal in Homeo, LPS-IFNγ or IL-4 treated microglia. Scale bar: 5 μm. Note that CAMSAP2 signal is present in microglia processes in Homeo and IL-4 treated cells. **(D)** Plot showing maximum fluorescence intensity values of CAMSAP2 vs the radial distance from cell nucleus, obtained with radial profiling, in Homeo (n = 18 cells, green), LPS-IFNγ (n = 14 cells, magenta) or IL-4 (n = 19 cells, blue) treated microglia. Curve fit was performed using single exponential decay function. Insert: bar chart reporting the exponential decay constant values (K) for each condition (values are expressed as mean ± SEM from 4 independent experiments; *** p <0.001, ** p <0.01 One-way ANOVA – Tukey's multiple comparison test.

Altogether, these data indicate that homeostatic and alternatively activated microglia display a mixed MT polarity pattern resembling neuronal MTs in dendrites, and that the acquisition of an activated phenotype represents a unique example of remodeling of the MT cytoskeleton from an array of parallel non-centrosomal MTs to a radial array of MTs.

Homeostatic microglia nucleate non-centrosomal MTs from Golgi outposts

In most dividing and motile cells, the centrosome is responsible for MT nucleation and anchoring, leading to the formation of radial MT arrays in which all MT minus ends are attached to the centrosome, while MT plus ends extend towards the cell periphery. In contrast, in most differentiated, stationary and axially polarized cells, MTs are more stable and organized in non-centrosomal arrays that are non-radially anchored at the centrosome (Bartolini and Gundersen 2006). CAMSAP2 is necessary for the tethering of newly nucleated non-centrosomal MT minus ends during the establishment of polarity in many cell types (Tanaka *et al.* 2012, Yau *et al.* 2014, Martin *et al.* 2018).

We investigated the distribution of γ-tubulin, the major MT nucleator in eukaryotic cells, in homeostatic and reactive microglia

by confocal microscopy and found that while in homeostatic and alternatively activated cells γ-tubulin, in addition to the signal present at the centrosome, displayed a punctate signal along cellular processes, in activated microglia γ-tubulin signal was condensed at the centrosomal and pericentrosomal area (Figure 9A-D). Normalized radial profiling (Figure 9B) of γ-tubulin fluorescence intensity, used as a measure of γ-tubulin signal distribution inside the cell, normalizing at the maximum at the centrosome in order to better discriminate the intracellular distribution of the protein, confirmed that γ-tubulin signal decayed more rapidly at increasing distances from the perinuclear region in activated microglia compared to homeostatic and alternatively activated cells (Figure 9B). This was also visible in volumetric rendering of γ-tubulin signal in the three states (Figure 9C). On the other hand, signal at the centrosome was higher in activated microglia compared to homeostatic and alternatively activated microglia, suggesting a condensed signal in a pericentrosomal area in these cells (Figure 9D). This observation was confirmed by the analysis of γ-tubulin signal over the cell area (Figure 9E). Higher levels of γ-tubulin protein expression revealed by western blot of whole cell lysates in homeostatic and alternatively activated microglia (Figure 9F) confirmed the prominent presence of γ-tubulin in microglia processes and ramifications, with a redistribution of the signal accompanying microglia activation.
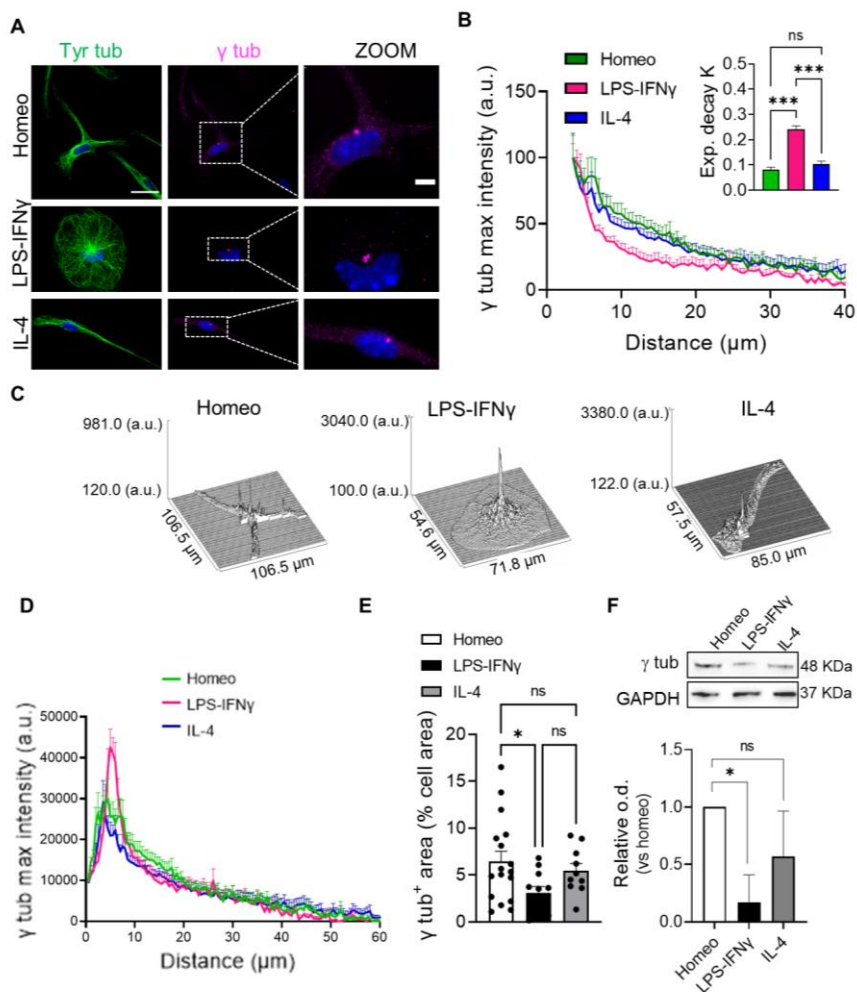
Fig. 9. Homeostatic, activated and alternatively activated primary microglia show different distribution of γ tubulin. (A) Representative IF images of homeostatic (Homeo), activated (LPS-IFNγ) and alternatively activated (IL-4) microglia stained for tyrosinated α-tubulin (Tyr tub, green) and γ-tubulin (γ tub, magenta; scale bar: 20 μm; zoom: 5 μm. Hoechst for nuclei visualization, blue). **(B)** Plot showing maximum fluorescence intensity values of γ tub vs the radial distance from cell nucleus, obtained with radial profiling, in Homeo (n = 13 cells, green), LPS-IFNγ (n = 14 cells, magenta) or IL-4 (n = 14 cells, blue) treated microglia. Curve fit was performed using single exponential decay function. Insert: bar chart reporting the exponential decay constant values (K) for each condition

(values are expressed as mean ± SEM from 3 independent experiments; *** p <0.001, One-way ANOVA – Tukey's multiple comparison). Note faster decay of γ tub signal in Activated microglia. **(C)** Representative volumetric rendering of γ tub signal intensity of Homeo condition and following LPS-IFNγ or IL4 treatment. **(D)** Maximum fluorescence intensity values of γ tub vs the radial distance from the center of the nucleus, obtained with radial profiling in Homeo (n = 13 cells, green), LPS-IFNγ (n = 14 cells, magenta) and IL-4 (n = 14 cells, blue) challenged microglia. **(E)** Scatter dot plot showing analysis of γ tub signal over the cell area in Homeo, LPS-IFNγ and IL-4 conditions. Values are expressed as mean ± SEM (Homeo n = 17, LPS-IFNγ n = 11 and IL-4 n = 10 cells from 4 independent experiments). * p <0.05, Kruskal-Wallis test - Dunn's multiple comparison test. **(F)** Representative immunoblot of total γ tub in Homeo, LPS-IFNγ and IL-4 treated microglia (*top*); bar chart showing the quantification of γ tub protein levels (*bottom*). Values are expressed as median ± interquartile range from 4 independent experiments. * p <0.05, Mann Whitney test.

Altogether, these data demonstrate that the acquisition of an activated phenotype is characterized by relocalization of γ-tubulin to a pericentrosomal area, which is necessary to establish radial MT arrays. The presence of relatively higher γ-tubulin signal in cell ramifications of homeostatic microglia further suggests that these microglia are alternatively enriched in non-centrosomal MT nucleation sites, which are necessary to establish non-centrosomal MT arrays.

Golgi outposts can serve as acentrosomal MTOCs in highly polarized brain cells, such as neurons and oligodendrocytes (Ori-McKenney *et al.* 2012, Fu *et al.* 2019, Valenzuela *et al.* 2020). We thus analyzed the distribution of the Golgi marker GM130, a scaffolding protein peripherally associated with Golgi membranes and a marker of Golgi outposts (Wu and Akhmanova 2017). Co-staining of GM130 with tyrosinated tubulin (Tyr tub) demonstrated the presence of isolated Golgi stacks in homeostatic microglia, while their presence was dramatically reduced in activated cells (Figure 10A and 10B). Importantly, most of the isolated GM130 positive stacks (73.6%) were decorated by γ-tubulin (Figure 10C). To determine whether Golgi outposts could function as MTOCs in homeostatic microglia, we evaluated MT nucleation by analyzing MT re-nucleation after nocodazole washout (Figure 10D). Nocodazole is a drug used to depolymerize MTs and disassemble the Golgi. We found that after 15 and 120 mins of nocodazole washout

to allow MT-regrowth and Golgi reassembly, MTs emerged from Golgi membranes (GM130 positive) both at pericentrosomal sites and at Golgi outposts located far from the centrosome (Figure 10E). Importantly, γ-tubulin was localized to nucleation-competent Golgi outposts, indicating that non-centrosomal MT re-nucleation did not occur spontaneously at these sites but was dependent on the presence of a γ-tubulin nucleation complex (Figure 10E).
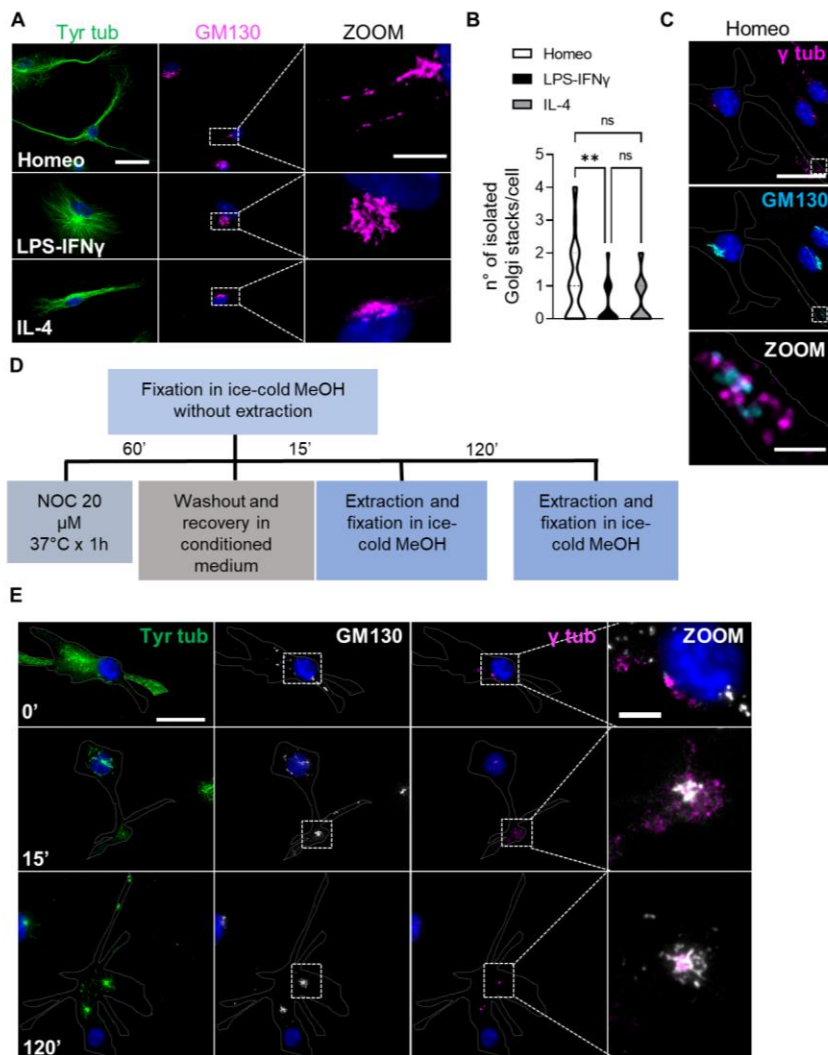
Fig. 10. Homeostatic microglia nucleate non-centrosomal MTs from Golgi outposts. (A) Representative confocal images showing co-staining of tyrosinated tubulin (Tyr tub, green) and GM130 (magenta) in homeostatic (Homeo), LPS-IFNγ or IL-4 treated microglia (scale bar: 20 μm; zoom: 5 μm. Hoechst for nuclei visualization, blue). **(B)** Violin plot showing number of isolated Golgi stacks per cell in the three phenotypes. Values are expressed as mean ± SEM of Homeo n = 57, LPS-IFNγ n = 34 and IL-4 n = 36 cells from 3 independent experiments. ** p <0.01. Kuskall-Wallis - Dunn's multiple comparison test. **(C)** Representative IF

images showing GM130 (cyan) and γ tub (magenta) staining in Homeo microglia. (Scale bar: 20 µm; zoom: 2 µm. Hoechst for nuclei visualization, blue). Note the presence of Golgi outposts in microglia processes. **(D)** Treatment timeline of Nocodazole wash out assay. **(E)** Representative confocal images of the time course of the MT re-nucleation assay after nocodazole washout in Homeo microglia stained for Tyr tub (green), GM130 (gray) and γ tub (magenta). Scale bar: 20 µm; zoom: 5 µm. Hoechst for nuclei visualization, blue. Time 0' represents the MT depolymerizing effect of nocodazole in homeostatic cells without free tubulin extraction. Note that MTs nucleate from distal Golgi outposts that are positive for γ-tubulin.

These data demonstrate that in homeostatic microglia Golgi outposts can function as sites of acentrosomal MT nucleation and suggest that non-centrosomal nucleation is necessary to establish an asymmetric MT array in these cells.

To assess whether these *in vitro* observations were representative of MT nucleation in microglia residing in tissue, we analyzed the subcellular distribution of GM130 in retinal microglia: retina and brain share a common embryological origin and similar cell types (Sernagor *et al.* 2001, Kavcic *et al.* 2011, Chang *et al.* 2014, Lee *et al.* 2014, Bambo *et al.* 2015, Javaid *et al.* 2016). Moreover, retinal neurons are arranged in distinct layers, and microglia are usually restricted to the retinal ganglion cell layer, thus offering an accessible structure for the imaging of their MT cytoskeleton. To identify the microglial cytoskeleton in retina we used cx3cr1[gfp/+] mice, which constitutively express GFP in microglia. As expected, retinal microglia from control cx3cr1[gfp/+] mice displayed a highly ramified morphology (Figure 11A), typical of homeostatic surveillant cells (Grimaldi *et al.* 2018, Basilico *et al.* 2019, Cordella *et al.* 2021). More importantly, confocal immunofluorescence analysis of GM130 signal in retinal GFP positive microglia confirmed the presence of isolated Golgi outposts also in the processes of homeostatic microglia residing in tissue (Figure 11C).
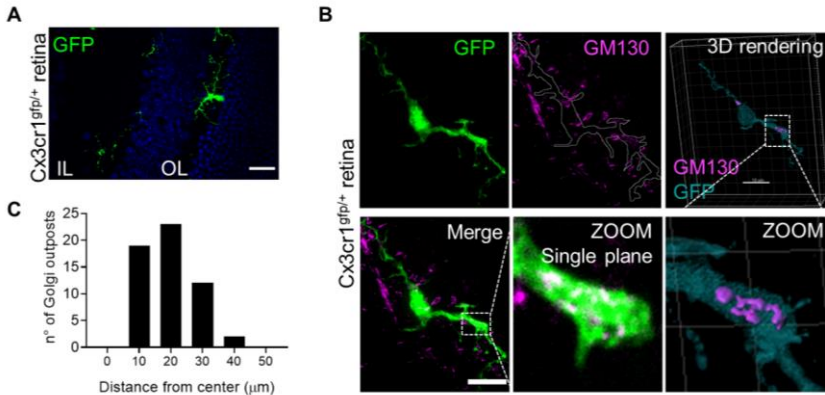
Fig. 11. Homeostatic microglia display Golgi outposts *in vivo*. (A) Representative images of retinal slices (50 μm thickness) from control cx3cr1[gfp/+] mice stained with Hoechst for nuclei visualization (blue), showing retinal cell layers (IL inner layer, OL outer layer). Scale bar: 20 μm. **(B)** *Left,* Representative z-projection confocal images of retinal slices (50 μm thickness) from cx3cr1[gfp/+] mice, expressing GFP in microglia cells, stained with GM130 (magenta) to visualize Golgi outposts. Scale bar: 5 μm. Zoom is a single confocal plane of a microglia ramification stained for GM130; scale bar: 5 μm. *Right*, 3D rendering of sample retinal GFP+ microglia (cyan) stained for GM130 (magenta). Scale bar: 10 μm, zoom: 5 μm. **(C)** Bar chart reporting the number of Golgi outposts at increasing distance from the center of cell body in retinal microglia.

Altogether, these results support the notion that MT organization in homeostatic microglia resembles the MT architecture typical of highly polarized cells and strongly suggest the presence of Golgi outposts as a hallmark of homeostatic microglia *in vitro* and *in vivo*.

Pericentrosomal redistribution of microtubule-nucleating material is a hallmark of activated microglia

The recruitment of pericentriolar material (PCM) to the centrosome has been described as a functional step for macrophage activation upon activating stimuli and was defined as "centrosomal

maturation" (Vertii *et al.* 2016). We thus investigated whether the recruitment of γ-tubulin to the pericentrosomal area was also a hallmark of activated microglia.

As revealed by super-resolution microscopy, activated microglia exhibited multiple γ-tubulin$^+$ dense puncta that localized to a perinuclear region (Figure 12A). Quantification of the number of γ-tubulin$^+$ puncta indicated that most activated cells had more than 3 puncta (70 ± 10%; Figure 12B). Conversely, almost all homeostatic and alternatively activated microglia displayed only 1 or 2 γ-tubulin$^+$ puncta (95 ± 3% and 96 ± 2%, respectively; Figure 12B). γ-tubulin localization to pericentrosomal puncta showed a time-dependent increase of both number and fluorescence integrated density upon LPS-INFγ challenge (Figure 12C). Importantly, recruitment of γ-tubulin$^+$ puncta was dependent on a dynamic MT cytoskeleton because a low dose of taxol was sufficient to inhibit it (Figure 12D and 12E).
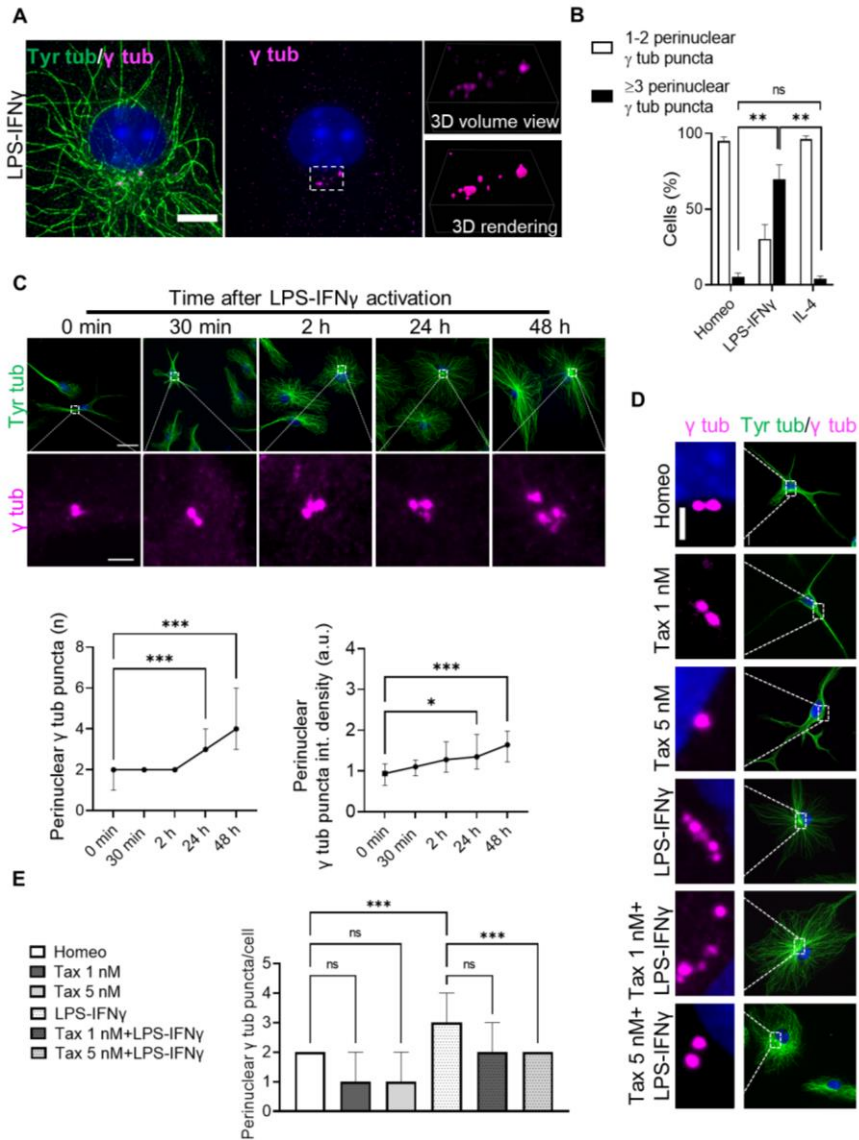
Fig. 12. Redistribution of pericentriolar material is a hallmark of activated microglia *in vitro*. **(A)** Representative confocal images showing γ-tubulin (γ tub) puncta (magenta) and tyrosinated α-tubulin (Tyr Tub, green) immunolabeling in activated (LPS-IFNγ) microglia (*left*, *middle*). Scale bar: 5 µm. Hoechst for nuclei visualization, blue. *Right:* relative volume view *(top)* and 3D rendering *(bottom)* of γ tub puncta (magenta) acquired via structured illumination microscopy. **(B)** Bar

chart reporting the percentage of cells displaying 1-2 γ tub puncta (white bars) or >3 γ tub puncta (black bars) in homeostatic (Homeo), activated (LPS-IFNγ) or alternatively activated (IL-4) microglia. Values are expressed as mean ± SEM from 3 independent experiments. ** p <0.01. One-way ANOVA - Dunnett's multiple comparison test. **(C)** *Top*: time course of γ tub redistribution during microglia activation: representative IF images showing γ tub (magenta) and tyrosinated α - tubulin (Tyr tub, green) staining at different time points (0 min, 30 min, 2 h, 24 h, 48 h). Scale bar: 20 µm; zoom, 2 µm. Hoechst for nuclei visualization, blue. *Bottom*: time course of number of γ tub puncta per cell (*left*) and quantification of γ tub puncta fluorescence intensity (*right*) during microglia activation. Values are expressed as median ± interquartile range (T0 n = 32; T30 min n = 40; T2h n = 44; T24h n = 41; T48h n = 33; from 3 independent experiments); *** p <0.001; ** p <0.01; * p <0.05, Kruskal-Wallis test - Dunn's multiple comparison test with respect to T0. **(D)** Representative IF images of tyrosinated Tyr tub (green) and γ tub (magenta) in homeostatic (Homeo), Taxol 1 nM treated (Tax 1 nM), Taxol 5 nM treated (Tax 5 nM), activated (LPS-IFNγ), Taxol 1 nM+LPS-IFNγ treated (Tax 1 nM+LPS-IFNγ) and Taxol 5 nM+LPS-IFNγ treated (Tax 5 nM+LPS-IFNγ) microglia (Scale bar: 10 µm; zoom, 2 µm. Hoechst for nuclei visualization, blue). **(E)** Bar chart reporting the number of γ tub puncta per cell in Homeo, Tax 1 nM, Tax 5nM, LPS-IFNγ, Tax 1 nM+LPS-IFNγ and Tax 5nM+LPS-IFNγ microglia. Values are expressed as median ± interquartile range from 3 independent experiments. ***p <0.001. Kruskall-Wallis - Dunn's multiple comparisons test.

Notably, in most activated cells with >2 γ-tubulin$^+$ puncta (65 ± 10%; Figure 13A) the centrosomal marker centrin-3 localized only to ≤2 γ-tubulin$^+$ puncta. In addition, while a quarter of activated cells was proliferating (23 ± 4%; Figure 13C and 13D), most activated microglia displayed >2 γ-tubulin$^+$ puncta (70 ± 10%; Figure 12B) and ≤2 centrin$^+$ puncta (Figure 13B).
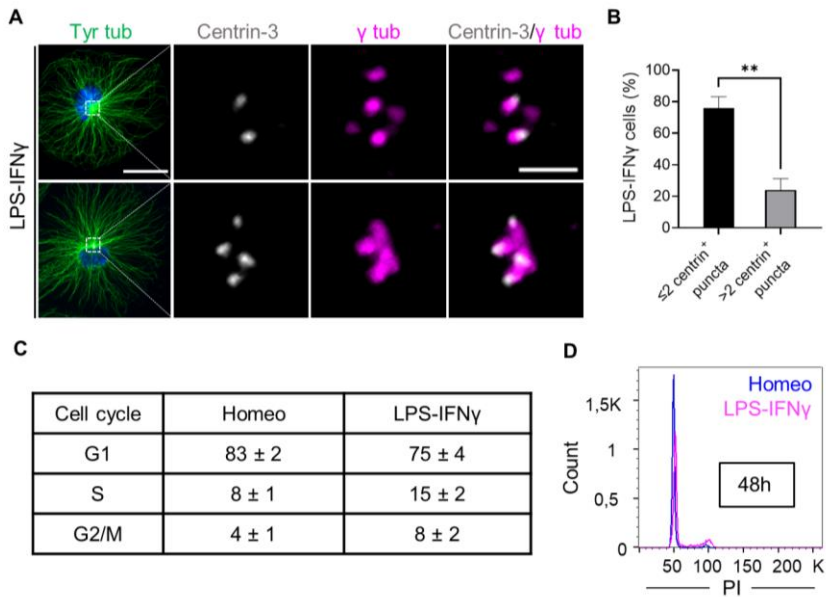
Fig. 13. Analysis of pericentriolar material maturation during microglia activation. (A) Representative images showing tyrosinated α-tubulin (Tyr tub, green), centrin-3 (gray) and γ -tubulin (γ tub, magenta) immunolabeling and co-localization of centrin-3 (gray) and γ tub (magenta) in activated (LPS-IFNγ) microglia. Scale bar: 20 μm; zoom, 2 μm. Hoechst for nuclei visualization, blue. **(B)** Bar graph reporting the percentage of LPS-IFNγ treated cells displaying ≤2 or >2 centrin$^+$ puncta. Values are expressed as mean ± SEM of n = 52 cells from 3 independent experiments. **p <0.01, Student's t-test. **(C)** Table reporting the percentage of cells in G1, S and G2/M phases from Homeo and LPS-IFNγ treated microglia cultures, stained with propidium iodide (PI) and analyzed by flow cytometry. Percentages indicate the relative enrichment in cell population, values are expressed as mean ± SEM from three independent experiments. **(D)** Representative histogram of cell cycle overlay of Homeo (blue line) and LPS-IFNγ (magenta line) treated microglia.

Conversely, PCM localization to γ-tubulin$^+$ puncta was confirmed by coimmunostaining with pericentrin (86 ± 5% of colocalizing puncta), a conserved PCM scaffold protein necessary for MTOC assembly and maturation (Zimmerman *et al.* 2004) (Figure 14A). Indeed, both centrin$^+$ and centrin$^-$ γ-tubulin$^+$ puncta localized to the center of MT asters (Fig. 14B) and MT re-growth after

nocodazole washout (Figure 14C and 14D) revealed that *de novo* MT nucleation occurred at γ-tubulin$^+$ puncta (Figure 14D). This indicated that γ-tubulin reorganization in activated microglia is ascribed to PCM maturation that is uncoupled from cell or centrosome duplication, and that γ-tubulin$^+$ puncta act as MTOCs.
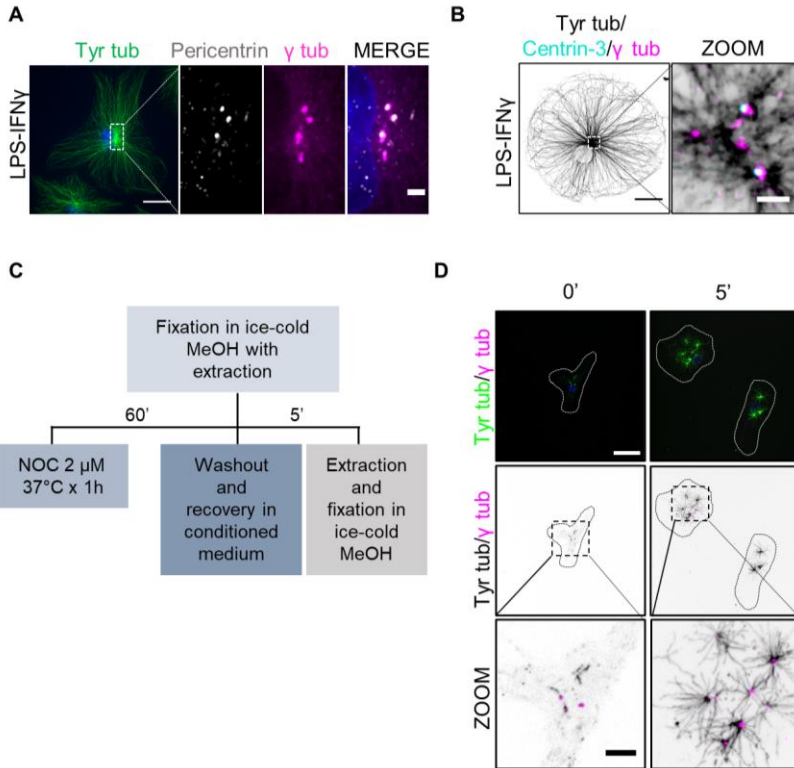
Fig. 14. Analysis of pericentriolar material maturation during microglia activation. (A) Images showing tyrosinated α-tubulin (Tyr tub, green), pericentrin (gray) and γ tub (magenta) immunolabeling in LPS-IFNγ treated microglia. Scale bar: 20 µm; zoom, 2 µm. Hoechst for nuclei visualization, blue. **(B)** Representative image showing Tyr tub (black, inverted LUT), centrin-3 (cyan) and γ tub (magenta) immunolabeling in LPS-IFNγ treated microglia. Out of focus blur was removed using "remove haze" filter in Metamorph Software to highlight the asters. Scale bar: 20 µm; zoom, 2 µm. Hoechst for nuclei visualization, blue. (**C**) Treatment timeline of Nocodazole wash out assay on LPS-IFNγ treated microglia. **(H)** Representative confocal images of the time course of the MT re-nucleation assay after nocodazole washout in LPS-IFNγ challenged microglia stained for Tyr tub

(green) and γ tub (magenta). Scale bar: 20 µm; zoom: 5 µm. Hoechst for nuclei visualization, blue. Time 0' represents the MT depolymerizing effect of nocodazole in LPS-IFNγ treated cells with free tubulin extraction.

Perinuclear γ-tubulin redistribution was also observed in activated microglia in a mouse model of retinal inflammation. For this, we took advantage of a well-established protocol of acute inflammatory uveitis (Becker *et al.* 2001, Rosenbaum *et al.* 2011, Wang *et al.* 2011, Chu *et al.* 2016, Bell *et al.* 2020, Wu *et al.* 2020) induced by intravitreal injection of LPS (Figure 15A) to activate retinal microglia towards the activated phenotype. Microglia in retinal slices from LPS-treated mice acquired an amoeboid morphology with reduced branching complexity, as revealed by skeleton analysis of Iba1 positive cells (Figure 15B and 15C).

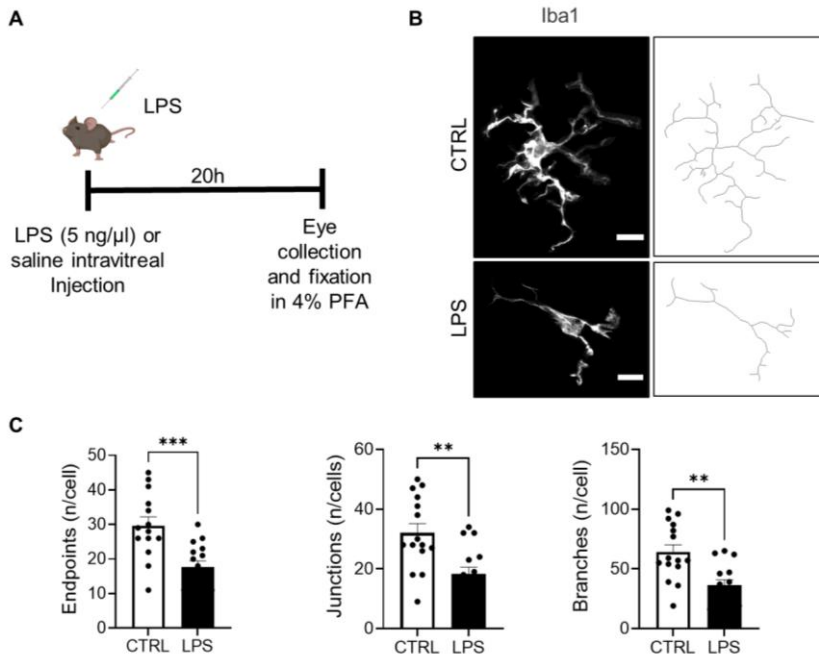

Fig 15. Characterization of *in vivo* microglia activation in the LPS-induced uveitis model. (A) Schematic illustration of surgical procedure and tissue collection. **(B)** *Left*: representative immunofluorescence images of microglia (Iba1,

gray) in retinal slices (50 µm thickness) from CTRL (sham) and LPS treated mice. Scale bar: 10 µm. *Right*: corresponding skeletonized images. **(C)** Scatter dot plots reporting microglia arborization parameters as endpoints (*left*), junctions (*middle*) and branches (*right*) obtained from skeleton analysis of retinal microglia from CTRL (sham) and LPS treated mice. Values are expressed as mean ± SEM (CTRL, n = 14/3 cells/mice; LPS, n = 15/3 cells/mice; *** p <0.001, ** p <0.01; Student's t-test.

Co-immunolabelling with Iba1 and γ-tubulin demonstrated that while in control (sham) mice retinal microglia displayed punctate diffuse γ-tubulin staining along cellular ramifications (Figure 16A), in LPS treated mice microglia clearly exhibited a condensed γ-tubulin pattern, clustered around a perinuclear region (Figure 16A). This was confirmed by quantitative analysis of γ-tubulin signal over the cell area and of the number of γ-tubulin$^+$ puncta per cell (Figure 16B).
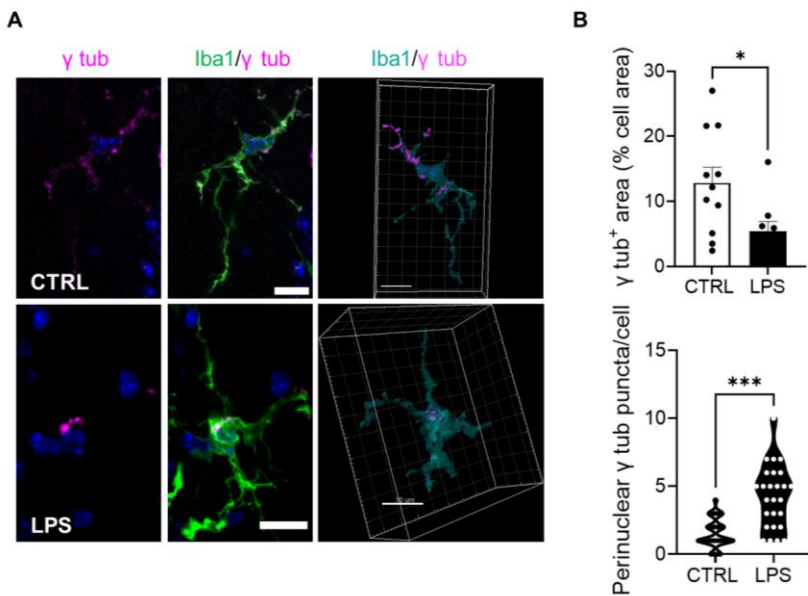
Fig 16. Redistribution of pericentriolar material is a hallmark of activated microglia *in vivo*. **(A)** *Left*: representative maximum intensity projections of images in retinal slices (50 μm thickness) from control (CTRL) mice stained for γ tub (magenta) and Iba-1 (green) antibodies (scale bar: 10 µm. Hoechst for nuclei visualization, blue). *Right*: 3D rendering highlighting the intracellular distribution of γ tub in CTRL (sham) and LPS treated mice. Scale bar: 10 µm. **(B)** *Top*: scatter

dot plot showing the γ tub signal over the cell area of retinal microglia from CTRL (sham) and LPS treated mice. Values are expressed as mean ± SEM of n = 11/3 cells/mice (CTRL) and n = 9/3 cells/mice (LPS). * p <0.05. Student's t-test. *Bottom*: violin plot showing the number of γ tub puncta per microglia in retinal slices from CTRL and LPS treated mice of n = 28/3 cells/mice (CTRL) and n = 26/3 cells/mice (LPS). *** p <0.001, Student's t-test.

In summary, these data demonstrate that the presence of pericentrosomal MTOC maturation is a *bona fide* feature of activated microglia *in vitro* and *in vivo*.

Next, we examined if maturation of pericentrosomal MTOCs was a regulatory step for microglia acquisition of the activated phenotype. To this end, we treated microglia with the selective PLK4 inhibitor centrinone to hamper PCM maturation (Yang *et al.* 2020), prior to LPS-INFγ stimulation (Figure 17A) and measured its effects on EV blebbing (Figure 17B). First, we found that centrinone increased the number (4.7-fold; Figure 17C, *top*) and reduced the diameter (by 30%; Figure 17C, *bottom*) of EVs blebbing from the cell surface of activated microglia (Figure 17B, 17C).
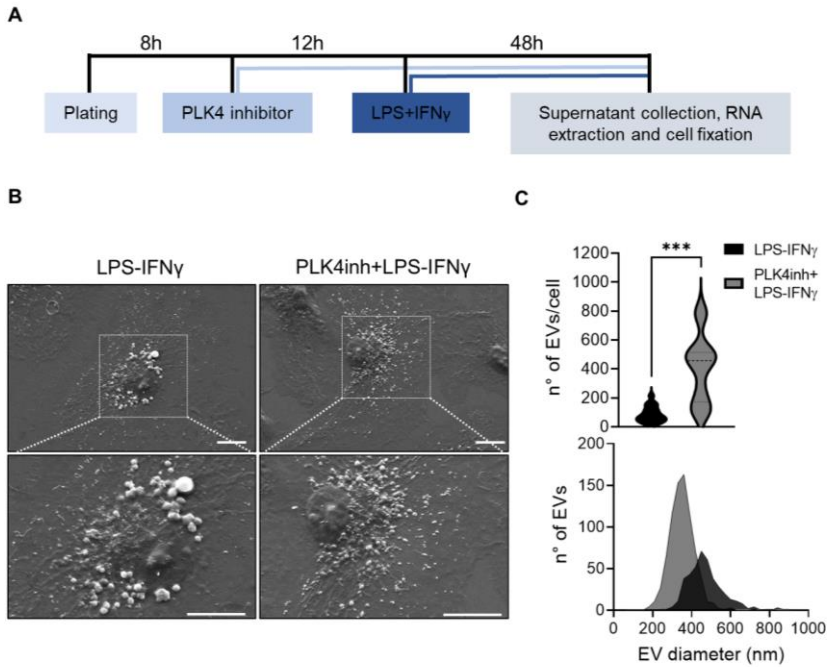
Fig. 17. Inhibition of pericentriolar material maturation alters the number and size of blebbing extracellular vesicles. (A) Experimental timeline of PLK4 inhibitor treatment and LPS-IFNγ administration. **(B)** Scanning electron micrographs showing extracellular vesicles (EVs) on the surface of LPS-IFNγ (*left*) and PLK4 inhibitor+LPS-IFNγ (*right*) treated microglia. Scale bar: 10 μm. **(C)** *Top*: violin plot showing the number of EVs in LPS-IFNγ challenged microglia with or without PLK4inh treatment (LPS-IFNγ n = 17 cells, PLK4 inhibitor+LPS-IFNγ n = 19 cells from 2 independent cultures; *** p <0.001, Student's t-test). *Bottom*: distribution of EV size measured on cell surface of LPS-IFNγ and PLK4 inhibitor+LPS-IFNγ treated microglia (LPS-IFNγ n = 17 cells, PLK4 inhibitor+LPS-IFNγ n = 19 cells).

Preliminary data: pericentrosomal redistribution of microtubule-nucleating material regulates IL-1β secretion

In response to specific activating stimuli, as for example LPS and extracellular ATP or nigericin, microglia and macrophages can activate NLRP3-inflammasome pathway (Gustin *et al.* 2015, Hanslik and Ulland 2020, Ji *et al.* 2021). Inflammasomes are innate immune

sensors that activate inflammatory caspases, thereby mediating maturation and secretion of the proinflammatory cytokines IL-1β and IL-18 (Schroder and Tschopp 2010, Davis *et al.* 2011, Latz *et al.* 2013).

The centrosome-associated protein kinase NEK7 is required for NLRP3–inflammasome activation (Seoane *et al.* 2020) and inhibition of PLK4 leads to NLRP3 hyper-activation through NEK7 dephosphorylation in bone marrow-derived macrophages (Yang *et al.* 2020).

Here, we measured NLRP3-inflammasome protein levels in homeostatic and activated microglia upon centrinone treatment. We found that in homeostatic microglia, LPS-IFNγ but not centrinone alone increased NLRP3 expression, while centrinone/LPS-IFNγ co-treatment enhanced NLRP3 more than LPS-IFNγ alone (Figure 18A). This suggests that inhibition of PLK4, inhibiting PCM maturation, may induce NLRP3 hyperactivation through NLRP3 oligomerization in activated microglia.

We then investigated whether PLK4 inhibition modulates microglia IL-1β expression and release, and found that co-treatment with centrinone significantly enhanced activated microglia-mediated IL-1β release (Figure 18C), but decreased IL-1β expression (Figure 18B), suggesting a possible negative feedback mechanism on IL-1β expression at the analyzed timepoint. In addition, we observed that centrinone did not modulate the release of IL-10 and IL-6 (Figure 18C), indicating that PLK4 inhibition may enhance activated microglia IL-1β release through NLRP3-inflammasome pathway activation without affecting NLRP3-independent pathways.
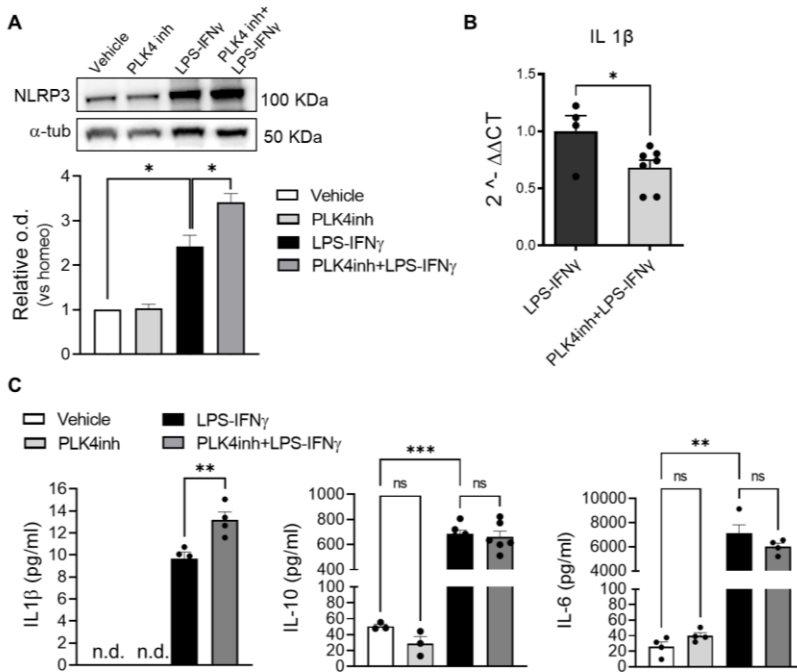
Fig 18. Inhibition of pericentriolar material maturation induces NLRP3 expression and IL1β secretion increase in activated microglia. (A) *Bottom*: bar chart reporting the amount of NLRP3 protein level in Vehicle, PLK4 inhibitor, LPS-IFNγ and PLK4 inhibitor+LPS-IFNγ microglia; *top*: representative immunoblot of NLRP3. Values are expressed as median ± interquartile range from 4 independent experiments, * p < 0.05, Mann Whitney test. **(B)** Scatter dot plot reporting Il-1β gene expression upon LPS-IFNγ or PLK4 inhibitor+LPS-IFNγ treatment, as revealed by RT-qPCR. Gene expression was normalized to the housekeeping gene *Gapdh,* n = 4 independent cultures. * p <0.05, Student's t-test. **(C)** Scatter dot plot showing protein quantification by ELISA of *left*: IL1β (n = 4 independent experiments, n.d. = non detectable), *middle*: IL-10 (Vehicle n = 3, PLK4inh n = 3, LPS-IFNγ n = 5 and PLK4 inhibitor+LPS-IFNγ n = 5 independent experiments) and *right*: IL-6 (n = 4 independent experiments). Values are expressed as mean ± SEM. For IL-1β: ** p < 0.01, Student's t-test. Note that supernatants from both Vehicle and PLK4 inhibitor microglia have undetectable levels of cytokine. For IL-10 and IL-6: *** p < 0.001, ** p < 0.01; One-way ANOVA - Holm-Šídák's multiple comparison test.

Together, these data suggest that remodeling of the MT cytoskeleton during microglia activation could be functionally

coupled to the regulation of cytokine release through a NEK7-NLRP3 inflammasome modulatory pathway.

Future perspectives

Microglia are pivotal mediators in neuroinflammation, and one of the first indications of neuroinflammation is microglia activation (Colonna and Butovsky 2017, Shabab *et al.* 2017). In Alzheimer's disease (AD), neuroinflammation contribute to the progression of the disease and, remarkably, in AD patients the Aβ senile plaque is often found to be in close proximity to reactive microglia (McGeer *et al.* 1988, Carpenter *et al.* 1993, Tarkowski *et al.* 2003, Wright *et al.* 2013). Therefore, finding new markers of microglial activation may help understand the underlying mechanisms of neuroinflammation in AD.

Gliosis in the brain is a typical hallmark of AD progression in many mouse models at different stages of the disease (Yokoyama *et al.* 2022), but recently the retina has emerged as a more accessible "window to the brain", as ocular manifestations of AD have been studied extensively over the past few decades (Parnell *et al.* 2012, Chang *et al.* 2014, Javaid *et al.* 2016, Grimaldi *et al.* 2019). TgCRND8 mice, a mouse model of amyloidopathy expressing the human Swedish (KM670/671NL) and Indiana (V717F) APP mutations, has been recently shown to display activated microglia in the retina at 9 months of age (Li *et al.* 2022).

Here we analyzed several morphological parameters in the retina of TgCRND8 mice, and found that none of the analyzed microglia morphological parameters in retinal slices from 7 months old TgCRND8 mice indicated activation compared to aged matched non transgenic controls (Figure 19).
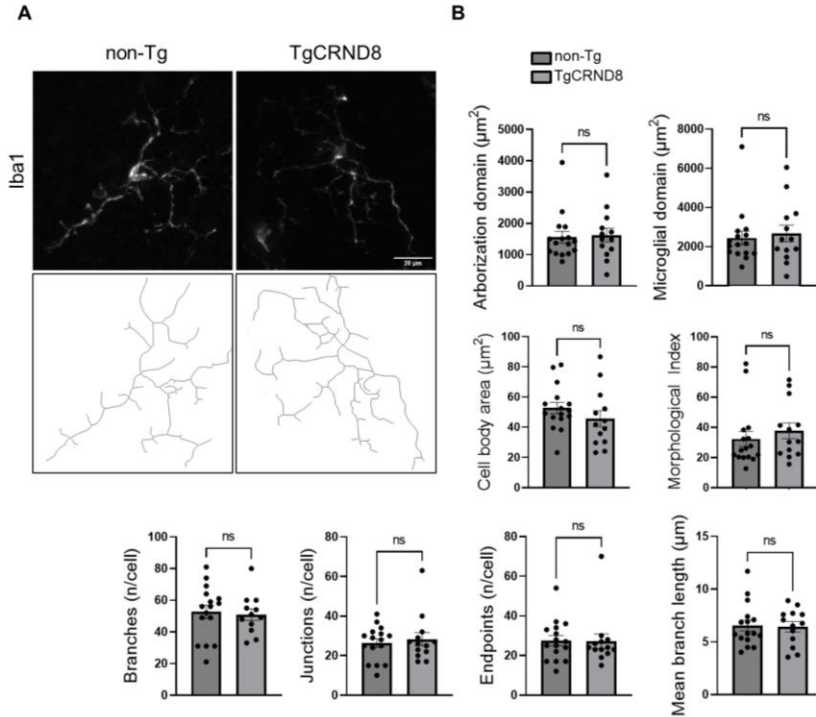
Fig 19. Characterization of retinal microglia morphology in TgCRND8 mice.
(A) *Top*: representative immunofluorescence images of microglia (Iba1, gray) in retinal slices (50 µm thickness) from 7 months old non-transgenic (non-Tg) and transgenic CRND8 (TgCRND8) mice. Scale bar: 20 µm. *Bottom*: corresponding skeletonized images. (B) Scatter dot plots reporting microglia morphological parameters: arborization and microglial domain (*top*), cell body area and morphological index (*middle*) and number of branches, junctions, endpoints and mean branch length (*bottom*) obtained from skeleton analysis of retinal microglia from 7 months old non-transgenic (non-Tg) and transgenic CRND8 (TgCRND8) mice. Values are expressed as mean ± SEM (non-Tg, n = 16/2 cells/mice; TgCRND8, n = 13/2 cells/mice; ns $p > 0.05$, Mann Whitney test).

Discussion

The results of this work show how microglia activation orchestrates a massive rearrangement of the microtubule cytoskeleton, and demonstrate the functional interplay between PCM maturation and microglia reactivity.

The study *in vitro* was conducted on primary microglia cells obtained from the cortex of newborn mice (postnatal day 0 to 2). The choice of primary murine microglia resides in the possibility to obtain a cell population more representative of microglia signature genes, physiology and morphology (Butovsky *et al.* 2014, Das *et al.* 2016) compared to immortalized cell lines. In particular, in physiological conditions, microglia in the CNS tissue are characterized by a small soma and highly ramified processes (Nimmerjahn *et al.* 2005, Kettenmann *et al.* 2011, Bernier *et al.* 2019); while this condition is extremely unlikely to be obtained *in vitro*, we managed to obtain 35% of ramified cells, defined as cells with $\geq$ 3 ramifications, a cell area comprised between 150 μm^2 and 1500 μm^2 and a solidity coefficient between 0.13 and 0.7. Microglia are prone to activate *in vitro* therefore, to minimize activation, we plated microglia cells at a low cell density (7×10^3 cells/cm^2) and with a low serum concentration (2.5% FBS) (Bohlen *et al.* 2017), and we avoided, when possible, infection or transfection techniques which appeared not to be well tolerated by the cultured cells. Microglia were treated with LPS-IFNγ or IL-4 to recapitulate activated or alternatively activated states (Gordon and Taylor 2005, Perry *et al.* 2010, Durafourt *et al.* 2012, Pagani *et al.* 2020): although we acknowledge that this paradigm is inadequate to describe microglia and macrophage activation *in vivo*, as microglia rarely display a dichotomic polarization towards either the activated or alternatively activated phenotype, our approach was functional to segregate three distinctive morphologies (ramified, amoeboid and bipolar), well recognizable also *in vivo* (Nimmerjahn *et al.* 2005, Orr *et al.* 2009, Tam and Ma 2014, Illes *et al.* 2020), and representative of the three different activation states. This allowed a better discrimination between the different reorganization states of the MT cytoskeleton. Nevertheless, we referred to the different reactive states as "activated" and "alternatively activated" to point

out the stimulation condition rather than the functional state of reactive microglia which is usually nuanced, while we defined "homeostatic" microglia the condition in absence of external triggering stimuli.

To date, only limited evidence has suggested that ramified microglia possess more acetylated and detyrosinated MTs than ameboid activated cells (Ilschner and Brandt 1996, Yu *et al.* 2018). Acetylation and detyrosination are two post-translational modification of α-tubulin often used as indirect indicators of more stable MTs (Webster and Borisy 1989, Baas *et al.* 2016) since once stabilized, MTs have sufficient longevity to be substrates for tubulin modifying enzymes. Here, we show that homeostatic ramified microglia display higher levels of tubulin acetylation and detyrosination.

Moreover, we report that during classical and alternative activation microglia MTs become less stable and more dynamic, since acetylation and detyrosination levels are decreased and MT dynamics parameters, obtained by analyzing SiR-tubulin labeled MTs, are increased. SiR-tubulin was chosen as a minimally invasive technique for live cell MT analysis, since these cells are difficult to transfect, making imaging of their cytoskeleton with genetically encoded probes challenging. These results suggest that the acquisition of new cellular functions induces changes in MT stability *via* modulation of MT dynamics (Li and Yang 2015), in line with what has been demonstrated in BV2 microglia (Yu *et al.* 2018) and, recently, in microglia *in vivo* (Möller *et al.* 2022), where light-mediated depolymerization of microtubules resulted in the acquisition of an amoeboid morphology and an alternative phagocytic strategy, suggesting that reducing microtubule stability may influence cell state, and that MT dynamicity is needed for correct microglia branch-mediated engulfment of apoptotic neurons (Möller *et al.* 2022).

We describe that homeostatic microglia MTs exhibit an asymmetric dendrite-like organization characterized by EB1 comets arranged in mixed polarity, suggested by the presence of a higher percentage of retrograde comets in transduced ramified cells expressing EB3-EGFP compared to the amoeboid cells. Notably, lentiviral expression of EB3-EGFP in homeostatic and alternatively

activated cells was low, while we had no success in infecting microglia that had been activated with LPS and IFNγ. In addition, in infected homeostatic microglia, values of cell area and solidity appeared slightly increased compared to non-infected cells, indicating that microglia reactivity might be affected by viral infection. Thus, we took advantage of an alternative approach: in non-infected cells we performed an analysis based on the comet-shaped accumulation of EB proteins at the MT minus ends, with comet tail intensity decaying exponentially after the maximum at the microtubule end that is toward the region of the microtubule lattice (Bieling *et al.* 2008, Mustyatsa *et al.* 2019): we took advantage of this property that allows to identify microtubule polarity on fixed cells by measuring fluorescence intensity gradients of EB positive comets with respect to the location of the nucleus. Although the gold standard techniques for measuring microtubule orientation remain live-cell imaging of EBs or the hooking technique (McIntosh and Euteneuer 1984), this easy and reproducible approach allows EB comet analysis on fixed cells, avoiding the challenge of transducing or transfecting microglia cells or relying on electron microscopy. Nevertheless, this approach was first validated by measuring fluorescence intensity gradients of EB comets from single frames of EB3-EGFP infected microglia movies, confirming that this approach was reliable to identify anterograde and retrograde direction of comets in microglia cells.

We thus describe that homeostatic microglial MTs in the ramifications exhibit an asymmetric organization characterized by EB1 bound plus ends arranged in mixed polarity in a dendrite-like manner: on the other side, we find that the minus-end capping protein CAMPSAP2 localized at branching points and cell ramifications. In alternatively activated microglia, we find lower levels of CAMSAP2 that localize in a similar fashion in bipolar processes. The presence of CAMSAP2 in microglia processes might suggest that stabilization of non-centrosomal MTs at their minus ends is important to achieve elongated bipolar morphology, typical of alternatively activated microglia, and for the formation of long branched cellular extensions patrolling brain parenchyma in homeostatic microglia, similar to what happens in neurons (Burton and Paige 1981, Heidemann *et al.* 1981, Baas *et al.* 1988, 1991, Jiang *et al.* 2014, Yau *et al.* 2014).

We find that the acquisition of an activated phenotype disrupts the cellular asymmetry of homeostatic microglia and reduces the pool of non-centrosomal, parallel and mixed oriented MTs, leading to their reorganization into a radial array of uniformly oriented MTs characteristic of the ameboid shape.

We then describe how microglia reactivity induces a redistribution of the nucleator protein γ-tubulin: from a diffuse pattern typical of homeostatic and alternatively activated cells, γ-tubulin is condensed in a perinuclear region in activated cells, where most of the MTs are anchored: although still present at the centrosome of homeostatic and alternatively activated cells, indicating a difference with the neuronal centrosomal loss of function as MTOC typical of neuronal maturation, γ-tubulin signal appears to be mostly localized to the pericentrosomal region in the activated state.

In addition, we find that homeostatic microglia nucleate acentrosomal MTs from Golgi outposts located far from the cell body inside microglia ramifications, resembling the structure of the dendritic tree of mature neurons (Horton *et al.* 2005, Nguyen *et al.* 2014, Yau *et al.* 2014) or the organization of oligodendrocytic myelin sheaths (Fu *et al.* 2019, Valenzuela *et al.* 2020). The sites of non-centrosomal renucleation in homeostatic microglia appear to be positive for γ-tubulin, suggesting that MT nucleation from Golgi outposts is dependent on γ-tubulin: nevertheless, to validate this hypothesis we should be able to inhibit γ-tubulin dependent nucleation. To this end, we set up a microtubule re-growth assay in the presence of the recently developed second generation γ-tubulin inhibitor Gatastatin G2 (Chinen *et al.* 2015, Shintani *et al.* 2020). However, the inhibitor in combination with the MT disassembling drug appeared not to be well tolerated by the cells, with a low rate of cell survival. Further studies are therefore needed to clarify the contribution of γ-tubulin in nucleating non-centrosomal MTs at Golgi outposts, alone or together with other possible candidates such as AKAP450 and CLASPs proteins (Efimov *et al.* 2007, Rivero *et al.* 2009).

The Golgi outpost-dependent non-centrosomal nucleation mechanism we show contrasts to activated and alternatively activated

microglia in which the Golgi apparatus displays a compact perinuclear location (Li *et al.* 2019), suggesting that in reactive microglia cellular arborization is reduced by restricting the Golgi to a region adjacent to the centrosome, which acts as the major MT nucleator in these cells. To further clarify this point, an additional experiment may be needed, consisting in a time course of microglia activation to observe the Golgi dynamics, to clarify if the Golgi outposts are recruited to the centrosome, possibly using motor protein machineries as carriers, or if they are degraded. We successfully expressed fluorescence proteins carried by recently developed adeno-associated viral vectors AAV-PHP.eB in cortical neurons of adult mice *via* retroorbital injections of small amount of viruses (Konno and Hirai 2020, Mathiesen *et al.* 2020): this minimally invasive approach might be useful for the analysis of this aspect of microglia physiology *in vivo* or in acute slices, after microglia activation *in situ*, designing a vector that carries GM130 and/or γ-tubulin under microglia specific promoters such as CX3CR1 or TMEM119.

We observed that the acquisition of an activated phenotype is characterized by γ-tubulin redistribution to puncta with increased γ-tubulin signal located to a perinuclear region, a feature we confirmed in retinal microglia residing in tissue. The presence of γ-tubulin positive puncta in the perinuclear region is correlating with the acquisition of a amoeboid morphology specifically after LPS-IFNγ activation, since amoeboid cells present in the cell culture in homeostatic conditions do not display this feature. This suggests that the machinery engaged for the reorganization of γ-tubulin at the centrosome might be triggered by specific cell signaling pathways.

Interestingly, γ-tubulin redistribution was strictly dependent on a dynamic MT cytoskeleton, suggesting that the increase in MT dynamicity is necessary for the relocation of MT nucleating material to the centrosome. Given the newly identified role for a population of spinal CD11c^{+} microglia in the remission and recurrence of neuropathic pain (Kohno *et al.* 2022), it will become critical to determine the contribution of spinal microglial MT dysfunction in the peripheral neuropathy caused by chemotherapeutic drugs, most of which target the MT cytoskeleton.

Importantly, γ-tubulin redistribution during the transition to an activated phenotype did not derive from centriolar duplication

during cell division (Fuller *et al.* 1995, Alvarado-Kristensson 2018) nor abnormal centriolar duplication (Nigg and Holland 2018), as no more than 2 γ-tubulin positive puncta colocalized with centrin-3, an abundant protein associated with the centrosome (Middendorp *et al.* 2000). A fascinating hypothesis on the nature of these γ-tubulin aggregates is that they might be part of a complex of centriolar satellites, small membrane-less granules that gravitate around the centrosome with functions in the maintenance of centrosomal homeostasis, cellular proteostasis and in ciliogenesis (Renaud and Bidère 2021). Staining with Pericentriolar Material 1 protein (PCM1) and other centriolar satellite proteins is therefore needed to test this hypothesis. Although reported in astrocytes and oligodendrocytes (Ki *et al.* 2021), the presence of primary cilia has not been demonstrated in macrophages, therefore their presence in microglia is unlikely. Nevertheless, this interpretation might provide new tools to characterize this γ-tubulin positive structures.

Co-localization of γ-tubulin with pericentrin confirms that these protein assemblies are composed of PCM and, interestingly, the *de novo* nucleation of radial MTs from γ-tubulin positive puncta after nocodazole washout strongly suggests their function as pericentrosomal MTOCs. A live-cell imaging analysis or time course for γ-tubulin recruitment during activation might be needed to further characterize the formation of pericentrosomal MTOCs. In light of recent studies (Möller *et al.* 2022), it has also to be considered a possible role for γ-tubulin positive puncta and PCM recruitment to the centrosome in phagocytosis, since the positioning of the centrosome is a regulatory factor in determining the rate of efferocytosis.

Importantly, the presence of γ-tubulin positive puncta in the perinuclear region of the cell is observed also in the retinal tissue in a model of local microglia activation after intravitreal injection of LPS. Therefore, our observations indicate that pericentrosomal redistribution of MT nucleating material may further provide a live-imaging marker of microglia activation to detect progression of neuroinflammatory disease and efficacy of therapeutics over time.

Our preliminary data also provide a possible functional cross-link between centrosome dynamics and cytokine release in activated

microglia. We find that PCM recruitment to the centrosome during activation, that may represent a form of centrosome maturation, negatively regulates IL-1β release through a non-classical secretory pathway (Lacy and Stow 2011). For this, we use the inhibitor of PLK4 (Wong *et al.* 2015), a microtubule-associated kinase fundamental in the regulation of cell cycle, that has been demonstrated to recruit γ-tubulin in the *de novo* formation of MTOCs (Montenegro Gouveia *et al.* 2019). We find that inhibition of PLK4 during microglia activation increases NLRP3 expression, and potentiates IL-1β release without affecting the release of IL-6 and IL-10, but in turn decreasing IL-1β transcript. Given that the NLRP3-inflammasome complex mediates IL-1β and IL-18 activation (Hanisch 2002, Schroder and Tschopp 2010, Lee *et al.* 2019, Seoane *et al.* 2020), NLRP3-inflammasome hyperactivation may account for the increase in IL-1β release and the accumulation of blebbing microvesicles we observe in microglia stimulated *in vitro*, negatively regulating IL-1β transcript in a negative feedback loop. In summary, our preliminary results show that PLK4 inhibition affects centrosomal maturation occurring during microglia activation, increasing NLRP3-inflammasome dependent IL-1β maturation and its release through microvesicles, suggesting centrosomal maturation as a negative regulator of IL-β release.

Several issues arise from these preliminary results: we acknowledge that to inhibit centrosome maturation the most appropriate kinase to target would be Plk1, since PLK4 is typically associated with centrosome duplication rather than centrosome maturation. However, in human macrophages the Plk1 inhibitor Bl2536 does not result in detectable decrease of LPS-induced recruitment of PCM proteins to the centrosome, suggesting that LPS-induced centrosome maturation in interphase macrophages may occur in a Plk1-independent way (Vertii *et al.* 2016). In addition, the role of PLK4 in recruiting PCM components, including γ-tubulin, promoting *de novo* MTOC formation (Montenegro Gouveia *et al.* 2019), indicates PLK4 inhibitor centrinone as a good candidate to target γ-tubulin-dependent centrosome maturation we observe in activated microglia. This though, in addition to the short duration of the centrinone treatment imposed by our delicate microglia culturing

conditions, preventing us to evaluate whether prolonged loss of PLK4 activity also resulted in inhibition of centrosome duplication and/or additional microglia specific effects, could account for the ambiguity of the results.

In addition, since NLRP3-inflammasome correct activation is mediated by the centrosomal protein NEK7, as NLRP3 hyperactivation is associated with NEK7 dephosphorilation caused by inhibition of PLK4 (Yang *et al.* 2020), our results might be integrated with the analysis of NEK7 role in centrosome maturation in activated microglia.

Finally, NLRP3 overexpression alone does not necessarily imply NLRP3 inflammasome activation, therefore further analysis of NLRP3 oligomerization and NLRP3-inflammasome activation markers, such as ASC or Caspase-1, is needed in order to validate these results. Also, LPS trigger alone is usually not sufficient to activate NLRP3-inflammasome, which typically requires a second triggering stimulus (e.g. nigericin, ATP) (Schroder and Tschopp 2010, Lee *et al.* 2019). Through P2X7 receptors, ATP plays an important role also in the biogenesis and dynamics of extracellular vesicles (Lombardi *et al.* 2021), through the NEK7-dependent activation of NLRP3 inflammasome: thus, it is compelling to investigate the role of centrosomal maturation in the biogenesis of microvesicles during microglia activation.

Interestingly, our results on cytokine release upon PLK4-inhibition differ from those reported after long-term (7 days) inhibition in macrophages activated with LPS (Vertii *et al.* 2016), where IL-10 and IL-6 release is decreased, suggesting that the response to loss of PLK4 activity is cell type specific or longer treatments may have either secondary or opposite effects. Further studies are necessary to discriminate between these possibilities.

In conclusion, these preliminary data pave the way to further investigation on how targeting PCM maturation in reactive microglia may represent a new approach to limit tissue damage during neurodegenerative diseases in which microgliosis contributes to neuronal injury and cognitive decline (Heneka *et al.* 2014, Colonna and Butovsky 2017).

As future direction, it would be interesting to investigate the role of microglia microtubule cytoskeleton in neurodegeneration. In

general, glial microtubules may contribute to the etiologies of myelinating diseases, aggregating neurodegenerative diseases, neurodevelopmental disorders, and neural injury (Weigel *et al.* 2020). In particular, in the context of neurodegenerative diseases when microglia become active driving neuroinflammation, such as Alzheimer's disease, (Perry *et al.* 2010, Subhramanyam *et al.* 2019) finding new markers of microglial activation may propose new diagnostic and/or therapeutic tools.

Gliosis has been shown in the brain of several AD mouse models at different stages of the disease (Yokoyama *et al.* 2022), but given the recent role of the retina as an accessible and consistent "window to the brain" (Parnell *et al.* 2012, Chang *et al.* 2014, Javaid *et al.* 2016, Grimaldi *et al.* 2019), and the feasibility of easily discriminating microglia cytoskeleton in the retina instead of using the densely packed parenchyma of the brain, retinal tissue appears to be the more appropriate model for our scope.

Here we find that none of the analyzed microglia morphological parameters in retinal slices from 7 months old TgCRND8 mice indicate activation compared to age-matched non transgenic controls. TgCRND8 mice overexpress the human APP gene with a double FAD-linked mutation, carrying the Swedish mutation (KM670/671NL) and the Indiana mutation (V717F) under the PrP gene promoter (Chishti *et al.* 2001). Deposition of Aβ in this mouse model starts from 3 months of age and becomes more extensive with age, with activated microglia appearing at 3 months of age, together with Aβ plaque accumulation (Dudal *et al.* 2004).

Nonetheless, the chosen age point may be still too early to observe neuroinflammation sufficient to induce clear morphological changes towards a more amoeboid form in activated microglia in the retina of these mice. Further studies on older mice (9 months) are needed in order to characterize microglia activation in this model, in terms of activation marker (CD68, IL1β) expression, microglia morphology and perinuclear γ-tubulin redistribution. In addition, further characterization is needed to clarify if this is the most appropriate model to investigate this issue.

Conclusions

In summary, our findings demonstrate that activated microglia orchestrate a heretofore unique example of microtubule cytoskeleton rearrangement, from a non-centrosomal array of stable MTs with mixed polarity nucleated at Golgi outposts, to a radial array in which MTs are uniformly oriented and anchored to *de novo* formed pericentrosomal MTOCs through their minus ends.

Our *in vitro* phenotyping and *in vivo* validation demonstrate that: homeostatic microglia display stable MT arrays, while microglia activation increases MT dynamicity; homeostatic microglia is characterized by non-centrosomal MT organization in arrays with mixed polarity, similar to the architecture typical of neurons and oligodendrocytes, despite the different embryonal origin; acentrosomal MT nucleation at Golgi outposts may play an important role in supporting the patrolling phenotype of microglia cells; microglia activation results in increased γ-tubulin and PCM localization to puncta around the centrosome, acting as MTOCs, providing a novel distinct marker of microglia activation; PCM maturation in activated microglia is inhibited by MT stabilization, representing a new approach to limit tissue damage during neurodegenerative diseases in which microgliosis contributes to neuronal injury and cognitive decline.

Materials and methods

Primary murine microglia culture and treatment

Primary cortical glial cells were prepared from 0- to 2-d-old mice as previously described (Rosito *et al.* 2012). Briefly, cerebral cortices were chopped and digested in 30 U/ml papain for 40 min at 37 °C followed by gentle trituration. The dissociated cells were washed, suspended in Dulbecco′s Modified Eagle′s Medium (DMEM, Sigma-Aldrich by Merck KGaA, Darmstadt, Germany) with 10% FBS (Gibco by Life Technologies, Carlsbad, CA, USA) and 2 mM L-glutamine and plated at a density of 9–10 x 105 in 175 cm^2 cell culture flasks. At confluence (10 –12 DIV), glial cells were shaken for 2 h at 37 °C to detach and collect microglial cells. These procedures gave an almost pure (<1% astrocyte contamination) microglial cell population. Microglia cells were plated at a density of $7x10^3$/cm^2 (to prevent cell contact activation) in astrocytes conditioned medium /DMEM 2,5% FBS (1:1). The day after plating microglia cells were treated for 48 h with IFNγ (20 ng/ml) and LPS (100 ng/ml) or with IL-4 (20 ng/ml) to obtain the activated or alternatively activated phenotype, respectively. To disassemble MTs, homeostatic and activated microglia were treated with 20 μM nocodazole (Sigma-Aldrich) added to the culture medium for 1 h at 37 °C. Samples were then kept on ice and washed 5x times with ice-cold medium. MTs were allowed to regrow in conditioned medium without nocodazole for 5 min or 15 min and 120 min at 37 °C. Right before fixation, free tubulin was rapidly extracted using a MT-preserving extraction buffer (60 mM PIPES, 25 mM HEPES, 10 mM EGTA, 2 mM MgCl$_2$, 0.1% saponin, pH 6.9 (Zhu and Kaverina 2011) for 20 sec at 37 °C. Cells were subsequently fixed with methanol at -20 °C for 4 min and processed for immunofluorescence staining. To stabilize MTs, microglia cells were treated for 24 h with 1 nM and 5 nM Taxol (Sigma-Aldrich) alone or together with IFNγ (20 ng/ml) and LPS (100 ng/ml). To inhibit PLK4, microglia cells were pre-treated with 125 nM Centrinone (Tocris) for 12 h prior to stimulation for 48 h with IFNγ (20 ng/ml) and LPS (100 ng/ml).

Immunofluorescence staining on fixed cells

Methanol fixation at -20 °C was elected for preserving an intact MT cytoskeleton: culture medium was removed and cells were fixed with pre-cooled 100% methanol at -20°C for 4 min prior to re-hydration with Phosphate-buffered saline (PBS, 0.01 M phosphate buffer, 0.0027 M potassium chloride and 0.137 M sodium chloride, pH 7.4, at 25 °C, Sigma-Aldrich) for at least 30 min at RT To preserve membrane associated components, cells were fixed with 4% paraformaldehyde (PFA)/PBS for 15 min at RT and then washed with PBS. When PFA fixed, cells were permeabilized with 0.1% Triton X-100/PBS for 1 to 3 min. After 2 washes in PBS, cells were blocked with 3% bovine serum albumin (BSA, Sigma-Aldrich) in PBS for 1 h at RT Primary antibodies (Rabbit Camsap1L1, Novus Biologicals, Englewood, CO, USA, 1:200; rabbit γ-tubulin, Invitrogen, Waltham, MA, USA, 1: 5000; mouse γ-tubulin, Sigma-Aldrich, 1:1000; rat Tyrosinated tubulin YL 1/2, Merck-Millipore, 1:1000; mouse Acetylated tubulin clone 6-11B-1, Sigma-Aldrich, 1:1000; mouse α-tubulin clone DM1A, Sigma-Aldrich, 1:500; rabbit Detyrosinated α-tubulin, Merck-Millipore, 1:1000; mouse EB1, BD Biosciences, San Jose, CA, USA 1:100; rabbit Pericentrin, Abcam, Cambridge, UK, 1:1500; mouse Centrin3, Abnova, Taipei City, Taiwan, 1:100; mouse GM130, BD Biosciences, 1:600; rabbit IBA-1, FujiFilm Wako, Richmond, VA, 1:300; Atto 488 Phalloidin, Sigma-Aldrich, 1:50) were incubated in 1.5% BSA in PBS for 2 h (RT) or overnight (+4°C). Cells were then extensively washed and stained with fluorophore-conjugated secondary antibodies in PBS (Alexa Fluor 488 goat anti-mouse, 488 goat anti-rat, 488 goat anti-rabbit, 594 goat anti-mouse, 647 goat anti-rabbit, Invitrogen; CF 594 goat anti-rat, Sigma-Aldrich; 1:500) and Hoechst (Sigma-Aldrich) for nuclei visualization for 1 h at RT prior to wash and mounting using Ibidi Mounting Medium. Cell outlines shown for display only were obtained by increasing the tubulin signal to identify the cell perimeter and are indicated by white dashed lines.

Lentiviral infection of microglia cells

Production of lentiviral particles was conducted using the 2nd generation packaging system as described in (Liu *et al.* 2014).

Briefly, HEK293T were transfected with lentiviral DNA plasmid and the packaging vectors pLP1, pLP2, and pLP-VSV-G (Thermo Fisher) using the calcium phosphate transfection method. At 24, 36, and 48 h after transfection, the virus was collected, filtered through 0.45 mm filter, and further concentrated using lentiviral precipitation solution as recommended by the manufacturer (ALSTEM). Concentrated virus was aliquoted and stored at -80°C.

EB3 comets analysis

Homeostatic microglia cells were infected with EB3-EGFP lentivirus the day after plating for 24 h and live-cell imaging of EB3 comets was performed (2 s/frame for 3 min) in astrocytes conditioned medium/DMEM 2,5% FBS (1:1) using an epifluorescence microscope (Nikon Eclipse Ti) equipped with an Orca II ER charge-coupled device (CCD) camera (Hamamatsu, Hamamatsu, Japan) and a temperature-controlled (37 °C) CO_2 incubator using a 60×/1.40NA objective . Kymographs were generated with ImageJ software.

Microtubule dynamics analysis

For live fluorescence imaging to measure MT dynamics, cells were incubated with 100 nM SiR-Tubulin (SpiroChrome, Stein-am-Rhein, Switzerland) at 37 °C for 30 min and washed with conditioned medium prior to visualization to improve signal to noise ratio. 10 µM Verapamil was added to inhibit efflux pumps and improve labeling. Live wide-field fluorescence imaging of SiRTub-labeled MTs was performed on an Olympus IX73 microscope, LDI laser source and CoolSNAP Myo camera, 4.54 µm pixels (Photometrics, Tucson, AZ, USA) with a built-in incubator, maintaining the temperature at 37 °C during recordings. Acquisitions were performed for 4 min (1 frame/4 sec) with a UPLSXAPO100x/1.45 oil objective and then analyzed with ImageJ software (see Image preparation and analysis).

Animals

All procedures performed using laboratory animals were in accordance with the Italian and European guidelines and were approved by the Italian Ministry of Health in accordance with the

guidelines on the ethical use of animals from the European Communities Council Directive of September 20, 2010 (2010/63/UE). All efforts were made to minimize suffering and number of animals used. Mice were housed in standard cages in a group of a maximum of 5 animals, with light–dark cycles of 12 h at 22±2 °C. Wild type C57BL-6 male and pregnant mice were purchased from Charles River and pups (P0-P2) were used to obtain primary glial cultures. Cx3cr1$^{gfp/gfp}$ male mice were purchased from The Jackson Laboratory company (B6.129P2(Cg)-Cx3cr1tm1Litt/J); the colony was established in our animal facility, and progenitors were bred to C57BL6J to obtain cx3cr1$^{gfp/+}$ mice as we previously reported (Pagani *et al.* 2015). Eyes from TgCRND8 and non-transgenic age-matched control mice were kindly provided from Paul Fraser.

Intravitreal injection and endotoxin induced uveitis

Adult C57BL6/J mice were intravitreally injected with sterile PBS (vehicle) or 5 ng/µl LPS from E. Coli (O55:B5, Sigma Aldrich). Intravitreal injection of LPS has been previously reported as a model of endotoxin induced uveitis (EIU) activating microglia in the retina (Becker *et al.* 2001, Rosenbaum *et al.* 2011, Wang *et al.* 2011, Chu *et al.* 2016, Bell *et al.* 2020). Animals were anaesthetized with 100 mg/kg methadomidine and 0.25 mg/kg ketamine. Pupils were dilated using 1% tropicamide and 2.5% phenylephrine (Chauvin, Essex, UK) and a small guide hole was made under the limbus with a 30G needle. The eye was gently massaged with a cotton swab to remove a portion of the vitreous to avoid a post-injection reflux of vitreous and/or drug solution. Then, 1 µl of vehicle or LPS solution was intravitreally injected through the initial hole using a 34G Hamilton syringe.

Immunofluorescence staining on retinal tissue

Cx3cr1$^{gfp/+}$ control mice were sacrificed at P70. CTRL (sham) and LPS intravitreally injected adult C57BL6/J mice were sacrificed 20 h after the injection procedure. TgCRND8 and non-transgenic age-matched control mice were sacrificed at 7 months. Eyes were removed and kept in 4% PFA solution overnight. Eyes were then cryoprotected in 30% sucrose and, after precipitation, frozen in

isopentane prior to storage at -80 °C. Frozen eyes were cut in 50-μm-thick sections with a Leica cryostat and processed for IF as published (Wu *et al.* 2020). Briefly, slices were immersed for 30 min in a boiling 1 mM EDTA solution (pH = 8.0) for antigen retrieval, then incubated with blocking solution (0.1% Triton X-100, 3% BSA and 0.05% Tween-20 in PBS) for 1 h at RT. Sections were incubated with primary antibodies (Iba1, FujiFilm Wako, 1:500; γ-tubulin, clone GTU-88, Sigma-Aldrich, 1:500; GM130, BD bioscience, 1:500) in diluted blocking solution overnight at 4 °C and 1 h at RT with fluorophore-conjugated secondary antibodies (Alexa Fluor 488 goat anti-rabbit, 594 goat anti-mouse) and Hoechst for nuclei visualization. The sections were mounted with anti-fade mounting medium (Invitrogen).

ELISA assay

To evaluate cytokine release, cell supernatant were analyzed with Mouse IL-6 Elisa Kit   (Invitrogen), Mouse IL-10 Elisa Kit (Invitrogen) and Mouse IL1β Elisa Kit   (Invitrogen)   after addition of 2% Triton X-100 to lysate the content of the vesicles.

Confocal Spinning Disk and Structured Illumination (SIM) microscopy

For fluorescence imaging of fixed samples, images were collected with spinning disk confocal microscopy on a Nikon Eclipse Ti equipped with X-Light V2 spinning disk (CrestOptics, Rome, Italy), combined with a VCS (Video Confocal Super resolution) module (CrestOptics) based on structured illumination, and a LDI laser source (89 North, Williston, VT, USA) and Prime BSI Scientific CMOS (sCMOS) camera, 6.5 µm pixels (Photometrics) or a CoolSNAP Myo camera, 4.54 µm pixels (Photometrics), with a 10x/0.25 NA Plan E air objective, 40x/0.75 PlanApo l air objective, a 60x/1.4 PlanApo l oil objective and a 100x/1.45 Plan E oil objective. The used Z step size was 0.2 µm for spinning disk and 0.1 µm for VCS. In order to achieve super-resolution, raw data obtained by the VCS module have been processed with a modified version of the joint Richardson-Lucy (jRL) algorithm (Ingaramo *et al.* 2014,

Ströhl and Kaminski 2015, Chakrova *et al.* 2016), where the out of focus contribution of the signal has been explicitly added in the image formation model used in the jRL algorithm, and evaluated as a pixel-wise linear "scaled subtraction" (Heintzmann and Benedetti 2006) of the raw signal. Retinal sections images were acquired on an Olympus IX73 microscope equipped with X-Light V3 spinning disk (CrestOptics), LDI laser source and a Prime BSI Scientific CMOS (sCMOS), 6.5 µm pixels (Photometrics) with a UPLSXAPO100x/1.45 oil objective. All the images were acquired by using Metamorph software version 7.10.2. (Molecular Devices, Wokingham, UK) and then analyzed with ImageJ software (see Image preparation and analysis).

Image preparation and analysis

For image preparation, we used the open-source software ImageJ (Schindelin *et al.* 2012) for adjustments of levels and contrast, maximum intensity projections, and thresholding signals for fluorescence intensity analysis.

Radial profile analysis. For tyrosinated α-tubulin, CAMSAP2 and γ-tubulin distribution analysis, microglia cells were fixed in methanol at -20 °C for 4 min or PFA 4% for 15 min and then stained with an anti-tyrosinated tubulin, CAMSAP2 or γ-tubulin antibody according to the immunofluorescence protocol, and Hoechst for nuclei visualization. Images obtained by confocal microscopy were analyzed with ImageJ to identify the coordinates of the center of the nucleus in each cell and to generate single-cell masks based on the morphology of each cell. A Python script was written to apply an Otsu threshold to the images (Otsu 1979) and to perform a radial scanning of fluorescence values, starting from the center of the nucleus of each cell, with a resolution of 0.065 μm. Maximum value radial profile was defined as the maximum fluorescence intensity (a.u.) for each concentric circle with an increasing distance from the nucleus center. For each analyzed cell the radial profile of the maximum value of fluorescence intensity (a.u.) was computed and plotted. Plots were smoothed with a resolution of 0.5 μm. All data points were exported into a Microsoft Excel 2010 compatible format. In CAMSAP2 analysis, only cytoplasmic staining was analyzed.

Curve fit was performed using a single exponential decay function on GraphPad Prism 9.0 (Y=(Y0 - Plateau)*exp(-K*X) + Plateau).

MT dynamics analysis. Analysis of MT dynamics was performed by tracing the lengths of the MTs via the "freehand line" tracing tool in ImageJ. Changes in length between successive frames were exported into an Excel sheet to determine the growth, shortening and pause events for each MT. Only changes >0.5 µm were considered growth or shortening events (Dhamodharan and Wadsworth 1995, Rusan *et al.* 2001). MT dynamics parameters were defined as follows: growth/shrinkage rate: distance (µm) covered in growth or shrinkage per second; % pause/growth/shrinkage: number of frames in pause/growth/shrinkage divided total number of frames X 100; catastrophe/rescue frequency (sec-1): number of catastrophe or rescue events divided by the product of the time of analysis and the percentage of growth or shrinkage; MT dynamicity: the sum of total length in growth and shortening divided by the time of analysis.

In vitro cell morphology analysis. Cell morphology analysis was performed using a quantitative measurement of cell area; cell solidity is expressed as the ratio between cell area and convex area. Measurements were obtained with the Particle Analysis tool and images were processed with ImageJ.

Extracellular vesicle analysis. For the statistical analysis of EV blebbing from the surface of microglia, 20 microglia cells per sample, collected in four different areas of the support, were randomly selected and scanned to count and measure the visualized vesicles. The ImageJ software was used to count and measure the vesicle major axis.

IF signal quantification. Cells were selected based on their representative morphology: ramified for homeostatic, ameboid for activated and bipolar for alternatively activated states. Detyr/Tyr tubulin ratio and Acetyl/Tyr tubulin ratio were calculated from the mean gray values of the respective IF signals, obtained from sum slices z-projections of 15 confocal planes after background subtraction (calculated as mean gray value of three circle background areas). EB1 anterograde or retrograde comets were defined from the EB1 fluorescence signal gradient from single plane images, measured with the "plot profile" tool of ImageJ. For Golgi stacks analysis, GM130 maximum intensity z-projection IF images were uniformly

thresholded on ImageJ by setting the same minimum values ('Default' threshold) to identify single Golgi stacks; a single Golgi stack was defined as a non-round object (roundness < 0.9) with a major axis length > 0.5 µm. For GM130- γ-tubulin co-staining analysis, GM130 and tubulin signals from max intensity z-projections were uniformly processed among different images increasing the 'brightness' and 'contrast' parameters by the same percentage. γ-tubulin signal over cell area was calculated as percentage of cell area covered by γ-tubulin signal; γ-tubulin signal threshold was uniformly applied on MetaMorph analysis software by setting the same minimum values to all images. Two or more distinct γ-tubulin$^+$ puncta were identified by counting the peaks of fluorescence intensity on a linescan drawn through the centroid of each puncta using the free-hand tool on ImageJ; The Find Peaks ImageJ plugin was used to identify the peaks by setting the minimum peak amplitude value at 100 grey values. Puncta were identified in a 132x132 pixels pericentriolar region after uniformly thresholding max intensity z-projections ('Default' threshold); integrated density was calculated in ImageJ as mean gray value*thresholded area. Pericentrin and Centrin-3- γ-tubulin co-localization analysis was performed by defining Pericentrin and Centrin-3$^+$ puncta as described above for γ-tubulin$^+$ puncta.

Retinal microglia cell skeleton analysis. Morphology of microglia cells in retinal sections was analyzed on max intensity z-projections; only entirely visible cells inside the acquisition field were analyzed; cells were isolated and then skeletonized on binary images, using the dedicated ImageJ plug-in; branches, endpoints and junction number was calculated from the skeletonized image.

Real time PCR

RNA was extracted from microglia cells with the Quick RNA MiniPrep (Zymo Research, Freiburg, DE) and retrotranscribed with iScript Reverse Transcription Supermix for Real-time PCR (RT-PCR) (Bio-Rad, Hercules, CA, USA). RT-PCR was carried out using Sybr Green (Bio-Rad) according to the manufacturer's instructions. The PCR protocol consisted of 40 cycles of denaturation at 95 ◦C for 30 s and annealing/extension at 60 ◦C for 30 s. For quantification, the

comparative Threshold Cycle (Ct) method was used. The Ct values from each gene were normalized to the Ct value of GAPDH in the same RNA samples. Relative quantification was performed using the $2^{-\Delta\Delta Ct}$ method (Schmittgen and Livak 2008) and expressed as fold change in arbitrary values.

Scanning Electron Microscopy (SEM) analysis

Samples were fixed in a solution of 1.5% glutaraldehyde in 0.1 M cacodylate buffer for 2 h at RT and post-fixed in 1% osmium tetroxide in Milli q (MQ) H_2O for 2 h. After several washes in MQ H_2O, the samples were subsequently dehydrated in rising concentrations of ethanol in H_2O solutions (from 30% to 100%), 1:1 ethanol:hexamethyldisilazane (HMDS, Sigma-Aldrich) and 100% HMDS and dried overnight in air. Finally, the samples were sputtered with a 10 nm gold layer and analyzed using a JEOL JSM-6490LA SEM operating at 10 KV of accelerating voltage.

Western blot

Cells were lysed in Laemmli sample buffer and boiled at 95 °C for 5 min. Proteins were separated by 4-12% Bis-Tris gel (Invitrogen) and transferred onto nitrocellulose membrane. After blocking in 5% milk/TBS (Tris 20 mM, NaCl 150 mM), membranes were incubated with primary antibodies at 4 °C overnight prior to 1 h incubation with secondary antibodies and signal detected using a commercial chemiluminescent assay (Immun-Star WesternC Kit; Bio-Rad). Image acquisition was performed with ChemiDoc MP imaging system (Bio-Rad) and densitometric analysis was performed with Quantity One software (Bio-Rad).

Cell cycle analysis

Microglia were collected following trypsin treatment. Cells were rinsed twice with phosphate buffered saline (PBS pH 7.4) and collected by centrifugation. Pellets were resuspended in ice cold 70% ethanol and stored at 4 °C for 1 h. Cells were collected by centrifugation, rinsed twice in PBS and resuspended in 20 µg/ml propidium iodide (PI) in PBS with 50 µg/ml RNase A for a minimum

of 30 min. After PI incubation, Flow cytometry analysis of DNA content was performed and analyzed using a BD LSRFortessa (BD Biosciences). The percentage of cells in different phases of the cell cycle was determined using the FlowJo V10.7.1 computer software (TreeStar, Ashland, OR, USA). At least 10.000 events for each sample were acquired.

Statistical analysis

The n number for each experiment and details of statistical analyses are described in the figure legends or main text. Data are reported as mean ± SEM; when not normally distributed, data are reported as median ± interquartile range. Origin 6 and GraphPad Prism 9 software were used for statistical analysis. Normality tests were performed with Prism 9 and nonparametric tests were used when appropriate. Significant differences are indicated in the figures by * $p < 0.05$, ** $p < 0.01$, *** $p < 0.001$. Notable non-significant differences are indicated in the figures by ns.

Original code max Intensity Radial Profile

The following code was generated by Dr. Giorgio Gosti and it is available at https://github.com/ggosti/maxIntensityRadialProfile.

It is a Python script for computing the maximum intensity radial profile of cells from pictures. The "maximum intensity radial profile" is a profile plot of the maximum intensity pixel among concentric circles as a function of distance from a center in the image.

```python
1    import matplotlib.pyplot as plt
2    import matplotlib.image as mpimg
3    import numpy as np
4    from math import sqrt, atan2, pi as PI
5    from skimage.measure import moments,moments_central,inertia_tensor,
     inertia_tensor_eigvals,regionprops
6    from skimage.filters import threshold_otsu
7    import os
8
9
10   # computes the radial profile of mean,max,min
11   def radialMean(im,x0,y0,h,w,rs):
12       yy,xx=np.mgrid[0:h,0:w]
13       rr= np.sqrt((xx-x0)**2+(yy-y0)**2)
14       #rs = range(rmax)
15       means = []
16       maxs = []
17       mins = []
18
19       #plt.figure()
20       #plt.imshow(rr)
21       #plt.show()
22
23       for r in range(len(rs)):
24           #print(r)
25           mask = (np.uint32(rr)==r)
26           a=im[mask]
27           if len(a)>0:
28               means.append(a.mean())
29               maxs.append(a.max())
30               mins.append(a.min())
31       #rs = np.array(rs) * pixelSize
32       return means,maxs,mins
33
34   # computes the cell orientation
35   def orientation(inertia_tensor):
36       a, b, b, c = inertia_tensor.flat
37       if a - c == 0:
38           if b < 0:
39               return -PI / 4.
40           else:
41               return PI / 4.
42       else:
43           return 0.5 * atan2(-2 * b, c - a)
44
45   # computes image covariance and eigenvectors
46   #def covImg(im):
47   #    M = moments(im)
48   #    cx,cy = (M[1, 0] / M[0, 0], M[0, 1] / M[0, 0])
49   #    mu = moments_central(im,[cx,cy])
50   #    cov = inertia_tensor(im,mu)
51   #    eigvals,w = np.linalg.eigh(cov)
52   #    l1,l2 = np.clip(eigvals, 0, None, out=eigvals)
53   #    #lmin = min(l1,l2)
54   #    #lmax = max(l1,l2)
55   #    ec = np.sqrt(1 - l1 /l2)
56   #    ori = orientation(cov)
57   #    return cx,cy,cov,l1,l2,w,ec,ori
58
59   # computes profile and other measures for a cell given a mask of the cell
60   def runOneCell(position, maskFileName, folder, rs):
61       #positions = [[position[0],position[1]]]
62       #maskFileNames = [maskFileName]
63
64       imgName = folder+'/image.tif'
65       #print('imgName',imgName)
66       img = mpimg.imread(imgName)
67       #maxR = 1100
68
69       #print('dtype',img.dtype,'max',img.max())
70       h,w=img.shape
71       #print('w',w,'h',h)
```

```python
72
73      f,[[axA,axB,axC],[axD,axE,axF]]=plt.subplots(2,3)
74      imgplot = axA.imshow(img, cmap="gray")
75
76      thresh = threshold_otsu(img)
77      binary = img > thresh
78      img = img*binary
79      imgplot = axB.imshow(img, cmap="gray")
80
81      #names = []
82      #eccs = []
83      #sols = []
84      #profiles = []
85      #smProfiles = []
86
87      #for cid,(maskName,pos, rmax) in enumerate(zip(maskFileNames,positions,maxR)):
88      #names.append(maskFileName[:-4])
89      name = maskFileName[:-4]
90      #cellIds.append(cid)
91      #print('mask path',folder+"/"+maskFileName)
92      mask = mpimg.imread(folder+"/"+maskFileName)
93      if mask.ndim == 3: mask=mask[:,:,0]
94      #print('mask',folder+"/"+maskFileName,mask.shape)
95      #plt.figure()
96      #plt.imshow(mask)
97      #plt.show()
98
99      celli = img * (mask>0)
100     #plt.figure()
101     axC.set_title(maskFileName[:-4])
102     imgplot = axC.imshow(celli, cmap="gray")
103
104     x0, y0 = position
105     means,maxs,mins = radialMean(celli,x0,y0,h,w,rs)
106     #cy,cx,cov,l1,l2,w,ec,ori = covImg(celli)
107     #props = regionprops(np.uint(celli>0),celli)
108     #f,[ax1,ax2,ax3]=plt.subplots(1,3,sharex=True,sharey=True)
109     #ax1.set_title(maskFileName[:-4])
110     #ax2.imshow(props[0].image)
111     #ax1.imshow(props[0].intensity_image)
112     #ax3.imshow(props[0].convex_image)
113     #sol=np.sum(props[0].image)/np.sum(props[0].convex_image)
114     #print('props sum intensity',props[0].mean_intensity*props[0].area,np.sum(celli))
115     #print('props',props[0].weighted_centroid)
116     #print('props',props[0].inertia_tensor)
117     #print('cov',cov)
118     #print('eiv',l1,l2,w)
119     #print('ec',ec)
120     #print('cy,cx',cy,cx)
121     print('y0,x0',y0,x0)
122     #print('sol',np.sum(props[0].image),np.sum(props[0].convex_image),sol)
123     #eccs.append(ec)
124     #sols.append(sol)
125     #profiles.append(maxs)
126     #smProfiles.append(maxs)
127
128     maxRad, minRad, meanRad = rs[maxs.index(max(maxs))], rs[mins.index(max(mins))], rs
        [means.index(max(means))]
129
130     # Here you choose the value of the averaging in um
131     averageOver=0.5
132
133     div,tmp,thres,precRad=0.,0.,0.,0
134     tabAvgMax, tabRsAvgMax=[],[]
135     for i in range(len(maxs)):
136         if rs[i]>=precRad+averageOver:
137             precRad+=averageOver
138             tabRsAvgMax.append(precRad)
139             tabAvgMax.append(tmp/(div+1e-10))
140             tmp,div=0.,0.
141         tmp+=maxs[i]
142         div+=1
```

```
143
144     #Questa parte adesso non serve più?#############
145     #txt="Radius (um)\tIntensity\n"
146     #for i in range(len(tabAvgMax)):
147     #     a=round(tabRsAvgMax[i] * 2) / 2
148     #     b=round(tabAvgMax[i] * 2) / 2
149     #     txt+=str(a)+"\t"+str(b)+"\n"
150     #with open(folder+"/AvgInt_"+imgName.replace(folder+"/", "") + "_" +
        maskFileName.replace(".tif", "")+".xls", "w+") as f:
151     #     f.write(txt)
152     ###################################################
153
154     print("The radius with maximum intensity is:", maxRad, "microns (" +str(maxRad/
        pixelSize)+"pixels)")
155
156     fig, ax = plt.subplots()
157     ax.set_title(' '.join(imgName.split('/')[:2])+' ' +maskFileName)
158     ax.plot(np.array(rs)[:len(maxs)],maxs,label='max',linewidth=1)
159     ax.plot(maxRad, maxs[maxs.index(max(maxs))], "or", label="(d=%.2f $\mu m$ ;
        I=%.2f)" %(maxRad,max(maxs)), markersize=6)
160     ax.plot(tabRsAvgMax, tabAvgMax, linewidth=2)
161     #plt.plot(np.array(rs),means,label='mean',linewidth=0.7)
162     #rs_mins = rs
163     ## If you want to consider only the mins>0 and not =0, add this code:
164     #mins, rs_mins = [x for x in mins if x>0], [rs[i] for i in range(len(mins)) if
        mins[i]>0]
165     #plt.plot(np.array(rs_mins),mins,label='mins', linewidth=0.7)
166     ax.legend()
167     ax.set_xlabel(r"Radius ($\mu m$)")
168     ax.set_ylabel("Fluorescence Intensity (a.u.)")
169     plt.savefig(folder+"/Graph_"+name+".png", dpi=600)
170
171     fig, ax = plt.subplots()
172     #plt.title("")
173     imgplot = axD.imshow(celli, cmap="gray")
174     imgplot = ax.imshow(celli, cmap="gray")
175     ax.set_yticks([])
176     ax.set_xticks([])
177
178     print('max pixel ',maskFileName ,celli.max())
179     print('min pixel ',maskFileName ,celli[mask>0].min())
180     print('mean int',maskFileName,celli[mask>0].mean())
181
182     for rc in range(0,2100,77):
183         cir = plt.Circle((x0, y0), rc, fill=False, color='b')
184         ax.add_artist(cir)
185
186     cir = plt.Circle((x0, y0), maxRad/pixelSize, fill=False, color='r')
187     ax.add_artist(cir)
188
189     ax.plot(x0, y0, '.b', markersize=5)
190
191     #draw orientation
192     #x1 = cx + np.cos(ori-PI / 2.) * 2 * np.sqrt(12)
193     #y1 = cy - np.sin(ori-PI / 2.) * 2 * np.sqrt(12)
194     #x2 = cx - np.sin(ori-PI / 2.) * 2 * np.sqrt(11)
195     #y2 = cy - np.cos(ori-PI / 2.) * 2 * np.sqrt(11)
196     #ax.plot((cx, x1), (cy, y1), '-r', linewidth=2.5)
197     #ax.plot((cx, x2), (cy, y2), '-r', linewidth=2.5)
198     #ax.plot(cx, cy, '.g', markersize=15)
199
200     plt.savefig(folder+"/Circ_"+name+".png", dpi=600)
201     #plt.show()
202     #plt.close()
203     plt.close('all')
204
205     return name, maxs, tabAvgMax, tabRsAvgMax
206
207
208  if __name__ == "__main__":
209
210     #with open("eccSols.txt", "w") as f:
```

```python
211         #   f.write('day \t folder \t num \t eccentricity \t solidity \n')
212
213         rmax = 2000
214         pixelSize = 0.065 #size of the pixel in microns
215         rs = np.arange(rmax+1) * pixelSize
216         with open("profiles.txt", "w") as f:
217             f.write('day \t folder \t num')
218             for r in rs:
219                 f.write('\t' + '{0:.3f}'.format(r))
220             f.write('\n')
221
222         rsSmooth = np.arange(0.5,(rmax + 1)*pixelSize,0.5)
223         with open("profilesSmooth.txt", "w") as f:
224             f.write('day \t folder \t num')
225             for r in rsSmooth:
226                 f.write('\t' + '{0:.3f}'.format(r))
227             f.write('\n')
228
229         days = [day for day in os.listdir() if os.path.isdir(day) and not ('.' in day) ]
230         print('days',days)
231
232         for day in days:
233             print('day',day)
234             dicPos={}
235             with open(day+"/coordinates.txt", "r") as f:
236                 for l in f:
237                     try:
238                         (folder, name, posx, posy) = l.replace("\n", "").split("\t")
239                     except ValueError:
240                         print("Oops! There is a problem with the coordinates.txt file.
                              Try and fix it...")
241                     posx, posy = float(posx), float(posy)
242                     try:
243                         dicPos[folder][name]=[posx, posy]
244                     except:
245                         dicPos[folder]={}
246                         dicPos[folder][name]=[posx, posy]
247
248
249             print('dicPos',dicPos.keys())
250             #print('dicPos[M0_2]',dicPos['M0_2'].keys())
251             #print('dicPos[M0_2][cell1]',dicPos['M0_2']['cell1'])
252
253             folders = [name for name in os.listdir(day)]
254             print('folders',folders)
255             for folder in folders:
256                 if folder not in dicPos:
257                     continue
258
259                 files = [name for name in os.listdir(day+'/'+folder)]
260
261                 for file in files:
262                     if "cell" not in file or ".tif" not in file or "xls" in file:
263                         continue
264                     file = file.replace(".tif", "")
265                     if file not in dicPos[folder]:
266                         continue
267
268                     #print('path to get stuff', folder, file)
269                     name, maxs, profilesSmooth, profilesSmoothRs = runOneCell(dicPos[
                          folder][file], file+".tif", day+'/'+folder, rs)
270
271                     #print('rsSmooth')
272                     #print(rsSmooth)
273                     #print(profilesSmoothRs)
274                     #with open("eccSols.txt", "a") as f:
275                     #    #print(day,name,ecc,sol)
276                     #
                         f.write(day+'\t'+folder+'\t'+str(name)+'\t'+str(ecc)+'\t'+str(sol)+'\n
                         ')
277
278                     with open("profiles.txt", "a") as f:
```

```python
279                    #print(name)
280                    f.write( day +'\t'+ folder + '\t' + str(name))
281                    for m in maxs:
282                        f.write('\t' + str(m))
283                    f.write('\n')
284
285
286                with open("profilesSmooth.txt", "a") as f:
287                    #print(name)
288                    f.write( day +'\t'+ folder + '\t' + str(name))
289                    for m in profilesSmooth:
290                        f.write('\t' + str(m))
291                    f.write('\n')
292
```

References

Ajami, B., Bennett, J.L., Krieger, C., Tetzlaff, W., and Rossi, F.M.V., 2007. Local self-renewal can sustain CNS microglia maintenance and function throughout adult life. *Nature Neuroscience*, 10 (12), 1538–1543.

Akhmanova, A. and Hoogenraad, C.C., 2015. Microtubule minus-end-targeting proteins. *Current Biology*, 25 (4), R162–R171.

Akhmanova, A. and Kapitein, L.C., 2022. Mechanisms of microtubule organization in differentiated animal cells. *Nature Reviews Molecular Cell Biology*, 23 (8), 541–558.

Akhmanova, A. and Steinmetz, M.O., 2019. Microtubule minus-end regulation at a glance. *Journal of cell science*, 132 (11), 1–7.

Alieva, I.B., Berezinskaya, T., Borisy, G.G., and Vorobjev, I.A., 2015. Centrosome nucleates numerous ephemeral microtubules and only few of them participate in the radial array. *Cell Biology International*, 39 (11), 1203–1216.

Alvarado-Kristensson, M., 2018. Γ-Tubulin As a Signal-Transducing Molecule and Meshwork With Therapeutic Potential. *Signal Transduction and Targeted Therapy*, 3 (1), 1–6.

Andjelkovic, A. V., Nikolic, B., Pachter, J.S., and Zecevic, N., 1998. Macrophages/microglial cells in human central nervous system during development: An immunohistochemical study. *Brain Research*, 814 (1–2), 13–25.

Baas, P.W., Deitch, J.S., Black, M.M., and Banker, G.A., 1988. Polarity orientation of microtubules in hippocampal neurons: Uniformity in the axon and nonuniformity in the dendrite. *Proceedings of the National Academy of Sciences of the United States of America*, 85 (21), 8335–8339.

Baas, P.W., Rao, A.N., Matamoros, A.J., and Leo, L., 2016. Stability properties of neuronal microtubules. *Cytoskeleton*, 73 (9), 442–460.

Baas, P.W., Slaughter, T., Brown, A., and Black, M.M., 1991. Microtubule dynamics in axons and dendrites. *Journal of Neuroscience Research*, 30 (1), 134–153.

Bambo, M.P., Garcia-Martin, E., Otin, S., Pinilla, J., Larrosa, J.M., Polo, V., and Pablo, L.E., 2015. Visual function and retinal nerve fibre layer degeneration in patients with Alzheimer

disease: correlations with severity of dementia. *Acta Ophthalmologica*, 93 (6), e507–e508.

Bartolini, F. and Gundersen, G.G., 2006. Generation of noncentrosomal microtubule arrays. *Journal of Cell Science*, 119 (20), 4155–4163.

Basilico, B., Ferrucci, L., Ratano, P., Golia, M.T., Grimaldi, A., Rosito, M., Ferretti, V., Reverte, I., Sanchini, C., Marrone, M.C., Giubettini, M., De Turris, V., Salerno, D., Garofalo, S., St-Pierre, M.K., Carrier, M., Renzi, M., Pagani, F., Modi, B., Raspa, M., Scavizzi, F., Gross, C.T., Marinelli, S., Tremblay, M.È., Caprioli, D., Maggi, L., Limatola, C., Di Angelantonio, S., and Ragozzino, D., 2021. Microglia control glutamatergic synapses in the adult mouse hippocampus. *Glia*, (September), 1–23.

Basilico, B., Pagani, F., Grimaldi, A., Cortese, B., Di Angelantonio, S., Weinhard, L., Gross, C., Limatola, C., Maggi, L., and Ragozzino, D., 2019. Microglia shape presynaptic properties at developing glutamatergic synapses. *Glia*, 67 (1), 53–67.

Becker, M.D., Garman, K., Whitcup, S.M., Planck, S.R., and Rosenbaum, J.T., 2001. Inhibition of leukocyte sticking and infiltration, but not rolling, by antibodies to ICAM-1 and LFA-1 in murine endotoxin-induced uveitis. *Investigative Ophthalmology and Visual Science*, 42 (11), 2563–2566.

Bell, O.H., Copland, D.A., Ward, A., Nicholson, L.B., Lange, C.A.K., Chu, C.J., and Dick, A.D., 2020. Single Eye mRNA-Seq Reveals Normalisation of the Retinal Microglial Transcriptome Following Acute Inflammation. *Frontiers in Immunology*, 10 (January).

Bernier, L.P., Bohlen, C.J., York, E.M., Choi, H.B., Kamyabi, A., Dissing-Olesen, L., Hefendehl, J.K., Collins, H.Y., Stevens, B., Barres, B.A., and MacVicar, B.A., 2019. Nanoscale Surveillance of the Brain by Microglia via cAMP-Regulated Filopodia. *Cell Reports*, 27 (10), 2895-2908.e4.

Bieling, P., Kandels-Lewis, S., Telley, I.A., Van Dijk, J., Janke, C., and Surrey, T., 2008. CLIP-170 tracks growing microtubule ends by dynamically recognizing composite EB1/tubulinbinding sites. *Journal of Cell Biology*, 183 (7), 1223–1233.

Bohlen, C.J., Bennett, F.C., Tucker, A.F., Collins, H.Y., Mulinyawe, S.B., and Barres, B.A., 2017. Diverse Requirements for Microglial Survival, Specification, and Function Revealed by Defined-Medium Cultures. *Neuron*, 94 (4), 759-773.e8.

Bolasco, G., Weinhard, L., Boissonnet, T., Neujahr, R., and Gross, C.T., 2018. Three-dimensional nanostructure of an intact microglia cell. *Frontiers in Neuroanatomy*, 12 (December), 1–5.

Burton, P.R. and Paige, J.L., 1981. Polarity of axoplasmic microtubules in the olfactory nerve of the frog. *Proceedings of the National Academy of Sciences*, 78 (5), 3269–3273.

Butovsky, O., Jedrychowski, M.P., Moore, C.S., Cialic, R., Lanser, A.J., Gabriely, G., Koeglsperger, T., Dake, B., Wu, P.M., Doykan, C.E., Fanek, Z., Liu, L., Chen, Z., Rothstein, J.D., Ransohoff, R.M., Gygi, S.P., Antel, J.P., and Weiner, H.L., 2014. Identification of a unique TGF-β-dependent molecular and functional signature in microglia. *Nature Neuroscience*, 17 (1), 131–143.

Carpenter, A.F., Carpenter, P.W., and Markesbery, W.R., 1993. Morphometric Analysis of Microglia in Alzheimer's Disease. *Journal of Neuropathology and Experimental Neurology*, 52 (6), 601–608.

Chakrova, N., Rieger, B., and Stallinga, S., 2016. Deconvolution methods for structured illumination microscopy. *Journal of the Optical Society of America A*, 33 (7), B12.

Chang, L.Y.L., Lowe, J., Ardiles, A., Lim, J., Grey, A.C., Robertson, K., Danesh-Meyer, H., Palacios, A.G., and Acosta, M.L., 2014. Alzheimer's disease in the human eye. Clinical tests that identify ocular and visual information processing deficit as biomarkers. *Alzheimer's and Dementia*, 10 (2), 251–261.

Cherry, J.D., Olschowka, J.A., and O'Banion, M.K., 2014. Neuroinflammation and M2 microglia: The good, the bad, and the inflamed. *Journal of Neuroinflammation*, 11 (1), 1–15.

Chinen, T., Liu, P., Shioda, S., Pagel, J., Cerikan, B., Lin, T.C., Gruss, O., Hayashi, Y., Takeno, H., Shima, T., Okada, Y., Hayakawa, I., Hayashi, Y., Kigoshi, H., Usui, T., and Schiebel, E., 2015. The γ-tubulin-specific inhibitor gatastatin reveals temporal requirements of microtubule nucleation during the cell

cycle. *Nature Communications*, 6, 2–11.

Chishti, M.A., Yang, D.S., Janus, C., Phinney, A.L., Horne, P., Pearson, J., Strome, R., Zuker, N., Loukides, J., French, J., Turner, S., Lozza, G., Grilli, M., Kunicki, S., Morissette, C., Paquette, J., Gervais, F., Bergeron, C., Fraser, P.E., Carlson, G.A., St. George-Hyslop, P., and Westawaya, D., 2001. Early-onset Amyloid Deposition and Cognitive Deficits in Transgenic Mice Expressing a Double Mutant Form of Amyloid Precursor Protein 695. *Journal of Biological Chemistry*, 276 (24), 21562–21570.

Chu, C.J., Gardner, P.J., Copland, D.A., Liyanage, S.E., Gonzalez-Cordero, A., Holthaus, S.M.K., Luhmann, U.F.O., Smith, A.J., Ali, R.R., and Dick, A.D., 2016. Multimodal analysis of ocular inflammation using the endotoxin-induced uveitis mouse model. *DMM Disease Models and Mechanisms*, 9 (4), 473–481.

Colonna, M. and Butovsky, O., 2017. Microglia function in the central nervous system during health and neurodegeneration. *Annual Review of Immunology*, 35, 441–468.

Conduit, P.T., Wainman, A., and Raff, J.W., 2015. Centrosome function and assembly in animal cells. *Nature Reviews Molecular Cell Biology*, 16 (10), 611–624.

Cordella, F., Sanchini, C., Rosito, M., Ferrucci, L., Pediconi, N., Cortese, B., Guerrieri, F., Pascucci, G.R., Antonangeli, F., Peruzzi, G., Giubettini, M., Basilico, B., Pagani, F., Grimaldi, A., D'Alessandro, G., Limatola, C., Ragozzino, D., and Di Angelantonio, S., 2021. Antibiotics Treatment Modulates Microglia–Synapses Interaction. *Cells*, 10 (10), 2648.

Das, A., Kim, S.H., Arifuzzaman, S., Yoon, T., Chai, J.C., Lee, Y.S., Park, K.S., Jung, K.H., and Chai, Y.G., 2016. Transcriptome sequencing reveals that LPS-triggered transcriptional responses in established microglia BV2 cell lines are poorly representative of primary microglia. *Journal of Neuroinflammation*, 13 (1), 1–18.

Das, R., Balmik, A.A., and Chinnathambi, S., 2020. Phagocytosis of full-length Tau oligomers by Actin-remodeling of activated microglia. *Journal of Neuroinflammation*, 17 (1), 1–15.

Davalos, D., Grutzendler, J., Yang, G., Kim, J. V., Zuo, Y., Jung, S., Littman, D.R., Dustin, M.L., and Gan, W.B., 2005. ATP

mediates rapid microglial response to local brain injury in vivo. *Nature Neuroscience*, 8 (6), 752–758.

Davis, B.K., Wen, H., and Ting, J.P.-Y., 2011. The Inflammasome NLRs in Immunity, Inflammation, and Associated Diseases. *Annual Review of Immunology*, 29 (1), 707–735.

Dhamodharan, R. and Wadsworth, P., 1995. Modulation of microtubule dynamic instability in vivo by brain microtubule associated proteins. *Journal of Cell Science*, 108 (4), 1679–1689.

Dudal, S., Krzywkowski, P., Paquette, J., Morissette, C., Lacombe, D., Tremblay, P., and Gervais, F., 2004. Inflammation occurs early during the Aβ deposition process in TgCRND8 mice. *Neurobiology of Aging*, 25 (7), 861–871.

Durafourt, B.A., Moore, C.S., Zammit, D.A., Johnson, T.A., Zaguia, F., Guiot, M.C., Bar-Or, A., and Antel, J.P., 2012. Comparison of polarization properties of human adult microglia and blood-derived macrophages. *Glia*, 60 (5), 717–727.

Efimov, A., Kharitonov, A., Efimova, N., Loncarek, J., Miller, P.M., Andreyeva, N., Gleeson, P., Galjart, N., Maia, A.R.R., McLeod, I.X., Yates, J.R., Maiato, H., Khodjakov, A., Akhmanova, A., and Kaverina, I., 2007. Asymmetric CLASP-Dependent Nucleation of Noncentrosomal Microtubules at the trans-Golgi Network. *Developmental Cell*, 12 (6), 917–930.

Etienne-Manneville, S., 2013. Microtubules in cell migration. *Annual Review of Cell and Developmental Biology*, 29, 471–499.

Eyo, U.B. and Wu, L.-J., 2019. Microglia: Lifelong Patrolling Immune Cells of the Brain. *Progress in Neurobiology*.

Fu, M. meng, McAlear, T.S., Nguyen, H., Oses-Prieto, J.A., Valenzuela, A., Shi, R.D., Perrino, J.J., Huang, T.T., Burlingame, A.L., Bechstedt, S., and Barres, B.A., 2019. The Golgi Outpost Protein TPPP Nucleates Microtubules and Is Critical for Myelination. *Cell*, 179 (1), 132-146.e14.

Fuller, S.D., Gowen, B.E., Reinsch, S., Sawyer, A., Buendia, B., Wepf, R., and Karsenti, E., 1995. The core of the mammalian centriole contains γ-tubulin. *Current Biology*, 5 (12), 1384–1393.

Gadadhar, S., Bodakuntla, S., Natarajan, K., and Janke, C., 2017. The tubulin code at a glance. *Journal of Cell Science*, 130 (8), 1347

LP – 1353.

Ginhoux, F., Greter, M., Leboeuf, M., Nandi, S., See, P., Gokhan, S., Mehler, M.F., Conway, S.J., Ng, L.G., Stanley, E.R., Samokhvalov, I.M., and Merad, M., 2010. Fate Mapping Analysis Reveals That Adult Microglia Derive from Primitive Macrophages. *Science*, 330 (6005), 841–845.

Gordon, S. and Taylor, P.R., 2005. Monocyte and macrophage heterogeneity. *Nature Reviews Immunology*, 5 (12), 953–964.

Graeber, M.B., Li, W., and Rodriguez, M.L., 2011. Role of microglia in CNS inflammation. *FEBS Letters*, 585 (23), 3798–3805.

Granucci, F., Petralia, F., Urbano, M., Citterio, S., Di Tota, F., Santambrogio, L., and Ricciardi-Castagnoli, P., 2003. The scavenger receptor MARCO mediates cytoskeleton rearrangements in dendritic cells and microglia. *Blood*, 102 (8), 2940–2947.

Grimaldi, A., Brighi, C., Peruzzi, G., Ragozzino, D., Bonanni, V., Limatola, C., Ruocco, G., and Di Angelantonio, S., 2018. Inflammation, neurodegeneration and protein aggregation in the retina as ocular biomarkers for Alzheimer's disease in the 3xTg-AD mouse model. *Cell Death and Disease*, 9 (6).

Grimaldi, A., Pediconi, N., Oieni, F., Pizzarelli, R., Rosito, M., Giubettini, M., Santini, T., Limatola, C., Ruocco, G., Ragozzino, D., and Di Angelantonio, S., 2019. Neuroinflammatory Processes, A1 Astrocyte Activation and Protein Aggregation in the Retina of Alzheimer's Disease Patients, Possible Biomarkers for Early Diagnosis. *Frontiers in Neuroscience*, 13 (September), 1–11.

Gustin, A., Kirchmeyer, M., Koncina, E., Felten, P., Losciuto, S., Heurtaux, T., Tardivel, A., Heuschling, P., and Dostert, C., 2015. NLRP3 inflammasome is expressed and functional in mouse brain microglia but not in astrocytes. *PLoS ONE*, 10 (6), 1–19.

Hanisch, U.K., 2002. Microglia as a source and target of cytokines. *Glia*, 40 (2), 140–155.

Hanslik, K.L. and Ulland, T.K., 2020. The Role of Microglia and the Nlrp3 Inflammasome in Alzheimer's Disease. *Frontiers in Neurology*, 11 (September), 1–9.

Heidemann, S.R., Landers, J.M., and Hamborg, M.A., 1981. Polarity

orientation of axonal microtubules. *Journal of Cell Biology*, 91 (3 I), 661–665.

Heintzmann, R. and Benedetti, P.A., 2006. High-resolution image reconstruction in fluorescence microscopy with patterned excitation. *Applied Optics*, 45 (20), 5037–5045.

Heneka, M.T., Kummer, M.P., and Latz, E., 2014. Innate immune activation in neurodegenerative disease. *Nature Reviews Immunology*, 14 (7), 463–477.

Herr, D.R., Yam, T.Y.A., Tan, W.S.D., Koh, S.S., Wong, W.S.F., Ong, W.Y., and Chayaburakul, K., 2020. Ultrastructural Characteristics of DHA-Induced Pyroptosis. *NeuroMolecular Medicine*, 22 (2), 293–303.

Hickman, S.E., Kingery, N.D., Ohsumi, T.K., Borowsky, M.L., Wang, L.C., Means, T.K., and El Khoury, J., 2013. The microglial sensome revealed by direct RNA sequencing. *Nature Neuroscience*, 16 (12), 1896–1905.

Horton, A.C., Rácz, B., Monson, E.E., Lin, A.L., Weinberg, R.J., and Ehlers, M.D., 2005. Polarized secretory trafficking directs cargo for asymmetric dendrite growth and morphogenesis. *Neuron*, 48 (5), 757–771.

Hua, J.Y. and Smith, S.J., 2004. Neural activity and the dynamics of central nervous system development. *Nature Neuroscience*, 7 (4), 327–332.

Illes, P., Rubini, P., Ulrich, H., Zhao, Y., and Tang, Y., 2020. Regulation of Microglial Functions by Purinergic Mechanisms in the Healthy and Diseased CNS. *Cells*, 9 (5), 1–24.

Ilschner, S. and Brandt, R., 1996. The transition of microglia to a ramified phenotype is associated with the formation of stable acetylated and detyrosinated microtubules. *Glia*, 18 (2), 129–140.

Ingaramo, M., York, A.G., Hoogendoorn, E., Postma, M., Shroff, H., and Patterson, G.H., 2014. Richardson-Lucy deconvolution as a general tool for combining images with complementary strengths. *ChemPhysChem*, 15 (4), 794–800.

Janke, C. and Bulinski, J.C., 2011. Post-translational regulation of the microtubule cytoskeleton: Mechanisms and functions. *Nature Reviews Molecular Cell Biology*, 12 (12), 773–786.

Janke, C. and Magiera, M.M., 2020. The tubulin code and its role in

controlling microtubule properties and functions. *Nature Reviews Molecular Cell Biology*, 21 (6), 307–326.

Javaid, F.Z., Brenton, J., Guo, L., and Cordeiro, M.F., 2016. Visual and ocular manifestations of Alzheimer's disease and their use as biomarkers for diagnosis and progression. *Frontiers in Neurology*, 7 (APR).

Ji, X., Song, Z., He, J., Guo, S., Chen, Y., Wang, H., Zhang, J., Xu, X., and Liu, J., 2021. NIMA-related kinase 7 amplifies NLRP3 inflammasome pro-inflammatory signaling in microglia/macrophages and mice models of spinal cord injury. *Experimental Cell Research*, 398 (2), 14–22.

Jiang, K., Hua, S., Mohan, R., Grigoriev, I., Yau, K.W., Liu, Q., Katrukha, E.A., Altelaar, A.F.M., Heck, A.J.R., Hoogenraad, C.C., and Akhmanova, A., 2014. Microtubule Minus-End Stabilization by Polymerization-Driven CAMSAP Deposition. *Developmental Cell*, 28 (3), 295–309.

Kassandra M. Ori-McKenney, Lily Yeh Jan, and Yuh-Nung Jan, 2012. Golgi outposts shape dendrite morphology by functioning as sites of acentrosomal microtubule nucleation in neurons. *Neuron*, 42 (1), 115–125.

Kavcic, V., Vaughn, W., and Duffy, C.J., 2011. Distinct visual motion processing impairments in aging and Alzheimer's disease. *Vision Research*, 51 (3), 386–395.

Kettenmann, H., 2007. The brain's garbage men. *Nature*, 446 (7139), 987–989.

Kettenmann, H., Hanisch, U.-K., Noda, M., and Verkhratsky, A., 2011. Physiology of Microglia. *Physiological Reviews*, 91 (2), 461–553.

Ki, S.M., Jeong, H.S., and Lee, J.E., 2021. Primary Cilia in Glial Cells: An Oasis in the Journey to Overcoming Neurodegenerative Diseases. *Frontiers in Neuroscience*, 15 (September), 1–19.

Kim, I., Mlsna, L.M., Yoon, S., Le, B., Yu, S., Xu, D., and Koh, S., 2015. A postnatal peak in microglial development in the mouse hippocampus is correlated with heightened sensitivity to seizure triggers. *Brain and Behavior*, 5 (12), 1–4.

Klinman, E. and Holzbaur, E.L.F., 2018. Walking Forward with Kinesin. *Trends in Neurosciences*, 41 (9), 555–556.

Kohno, K., Shirasaka, R., Yoshihara, K., Mikuriya, S., Tanaka, K., Takanami, K., Inoue, K., Sakamoto, H., Ohkawa, Y., Masuda, T., and Tsuda, M., 2022. A spinal microglia population involved in remitting and relapsing neuropathic pain. *Science (New York, N.Y.)*, 376 (6588), 86–90.

Konno, A. and Hirai, H., 2020. Efficient whole brain transduction by systemic infusion of minimally purified AAV-PHP.eB. *Journal of Neuroscience Methods*, 346 (April).

Lacy, P. and Stow, J.L., 2011. Cytokine release from innate immune cells: Association with diverse membrane trafficking pathways. *Blood*, 118 (1), 9–18.

Latz, E., Xiao, T.S., and Stutz, A., 2013. Activation and regulation of the inflammasomes. *Nature Reviews Immunology*, 13 (6), 397–411.

Lee, D.H., Laemmer, A.B., Waschbisch, A., Struffert, T., Maihöfner, C., Schwab, S., and Linker, R.A., 2014. Neuromyelitis optica presenting with relapses under treatment with natalizumab: A case report. *Journal of Medical Case Reports*, 8 (1), 2–4.

Lee, E., Hwang, I., Park, S., Hong, S., Hwang, B., Cho, Y., Son, J., and Yu, J.W., 2019. MPTP-driven NLRP3 inflammasome activation in microglia plays a central role in dopaminergic neurodegeneration. *Cell Death and Differentiation*, 26 (2), 213–228.

Lewis, T.L. and Polleux, F., 2012. Neuronal Morphogenesis: Golgi Outposts, Acentrosomal Microtubule Nucleation, and Dendritic Branching. *Neuron*, 76 (5), 862–864.

Li, J., Ahat, E., and Wang, Y., 2019. *Golgi structure and function in health, stress, and diseases*. Results and Problems in Cell Differentiation.

Li, L. and Yang, X.J., 2015. Tubulin acetylation: Responsible enzymes, biological functions and human diseases. *Cellular and Molecular Life Sciences*, 72 (22), 4237–4255.

Li, R. and Gundersen, G.G., 2008. Beyond polymer polarity: How the cytoskeleton builds a polarized cell. *Nature Reviews Molecular Cell Biology*, 9 (11), 860–873.

Li, R., Liang, Y., and Lin, B., 2022. Accumulation of systematic TPM1 mediates inflammation and neuronal remodeling by phosphorylating PKA and regulating the FABP5/NF-κB

signaling pathway in the retina of aged mice. *Aging Cell*, 21 (3), 1–23.

Liu, J., Pasini, S., Shelanski, M.L., and Greene, L.A., 2014. Activating transcription factor 4 (ATF4) modulates post-synaptic development and dendritic spine morphology. *Frontiers in Cellular Neuroscience*, 8 (JUN), 1–13.

Lombardi, M., Gabrielli, M., Adinolfi, E., and Verderio, C., 2021. Role of ATP in Extracellular Vesicle Biogenesis and Dynamics. *Frontiers in Pharmacology*, 12 (March), 1–8.

Lukinavičius, G., Reymond, L., D'Este, E., Masharina, A., Göttfert, F., Ta, H., Güther, A., Fournier, M., Rizzo, S., Waldmann, H., Blaukopf, C., Sommer, C., Gerlich, D.W., Arndt, H.D., Hell, S.W., and Johnsson, K., 2014. Fluorogenic probes for live-cell imaging of the cytoskeleton. *Nature Methods*, 11 (7), 731–733.

Madry, C., Kyrargyri, V., Arancibia-Cárcamo, I.L., Jolivet, R., Kohsaka, S., Bryan, R.M., and Attwell, D., 2018. Microglial Ramification, Surveillance, and Interleukin-1β Release Are Regulated by the Two-Pore Domain K+ Channel THIK-1. *Neuron*, 97 (2), 299-312.e6.

Martin, M., Veloso, A., Wu, J., Katrukha, E.A., and Akhmanova, A., 2018. Control of endothelial cell polarity and sprouting angiogenesis by noncentrosomal microtubules. *eLife*, 7, 1–37.

Mathiesen, S.N., Lock, J.L., Schoderboeck, L., Abraham, W.C., and Hughes, S.M., 2020. CNS Transduction Benefits of AAV-PHP.eB over AAV9 Are Dependent on Administration Route and Mouse Strain. *Molecular Therapy - Methods and Clinical Development*, 19 (December), 447–458.

McGeer, P.L., Itagaki, S., Tago, H., and McGeer, E.G., 1988. Occurrence of HLA-DR Reactive Microglia in Alzheimer's Disease. *Annals of the New York Academy of Sciences*, 540 (1 Advances in N), 319–323.

McIntosh, J.R. and Euteneuer, U., 1984. Tubulin hooks as probes for microtubule polarity: An analysis of the method and an evaluation of data on microtubule polarity in the mitotic spindle. *Journal of Cell Biology*, 98 (2), 525–533.

Meiring, J.C.M. and Akhmanova, A., 2020. Microtubules keep large cells in shape. *Journal of Cell Biology*, 219 (6), 1–3.

Middendorp, S., Küntziger, T., Abraham, Y., Holmes, S., Bordes, N.,

Paintrand, M., Paoletti, A., and Bornens, M., 2000. A role for centrin 3 in centrosome reproduction. *Journal of Cell Biology*, 148 (3), 405–415.

Mitchison, T. and Kirschner, M., 1984. Dynamic instability of microtubule growth. *Nature*, 312 (5991), 237–242.

Möller, K., Brambach, M., Villani, A., Gallo, E., Gilmour, D., and Peri, F., 2022. A role for the centrosome in regulating the rate of neuronal efferocytosis by microglia in vivo. *bioRxiv*, 2022.08.12.503784.

Montenegro Gouveia, S., Zitouni, S., Kong, D., Duarte, P., Gomes, B.F., Sousa, A.L., Tranfield, E.M., Hyman, A., Loncarek, J., and Bettencourt-Dias, M., 2019. PLK4 is a microtubule-associated protein that self-assembles promoting de novo MTOC formation. *Journal of Cell Science*, 132 (4).

Mustyatsa, V. V., Kostarev, A. V., Tvorogova, A. V., Ataullakhanov, F.I., Gudimchuk, N.B., and Vorobjev, I.A., 2019. Fine structure and dynamics of EB3 binding zones on microtubules in fibroblast cells. *Molecular Biology of the Cell*, 30 (17), 2105–2114.

Nguyen, M.M., McCracken, C.J., Milner, E.S., Goetschius, D.J., Weiner, A.T., Long, M.K., Michael, N.L., Munro, S., and Rolls, M.M., 2014. γ-tubulin controls neuronal microtubule polarity independently of Golgi outposts. *Molecular Biology of the Cell*, 25 (13), 2039–2050.

Nigg, E.A. and Holland, A.J., 2018. Once and only once : mechanisms of centriole duplication and their deregulation in disease. *Nature Publishing Group*, 19 (5), 297–312.

Nikodemova, M., Kimyon, R.S., De, I., Small, A.L., Collier, L.S., and Watters, J.J., 2015. Microglial numbers attain adult levels after undergoing a rapid decrease in cell number in the third postnatal week. *Journal of Neuroimmunology*, 278, 280–288.

Nimmerjahn, A., Kirchhoff, F., and Helmchen, F., 2005. Resting microglial cells are highly dynamic surveillants of brain parenchyma in vivo. *Neuroforum*, 11 (3), 95–96.

Nogales, E., Whittaker, M., Milligan, R.A., and Downing, K.H., 1999. High-resolution model of the microtubule. *Cell*, 96 (1), 79–88.

Ori-McKenney, K.M., Jan, L.Y., and Jan, Y.N., 2012. Golgi Outposts

Shape Dendrite Morphology by Functioning as Sites of Acentrosomal Microtubule Nucleation in Neurons. *Neuron*, 76 (5), 921–930.

Orr, A.G., Orr, A.L., Li, X.J., Gross, R.E., and Traynelis, S.F., 2009. Adenosine A2A receptor mediates microglial process retraction. *Nature Neuroscience*, 12 (7), 872–878.

Otsu, N., 1979. A Threshold Selection Method from Gray-Level Histograms. *IEEE Transactions on Systems, Man, and Cybernetics*, 9 (1), 62–66.

Pagani, F., Paolicelli, R.C., Murana, E., Cortese, B., Di Angelantonio, S., Zurolo, E., Guiducci, E., Ferreira, T.A., Garofalo, S., Catalano, M., D'Alessandroo, G., Porzia, A., Peruzzi, G., Mainiero, F., Limatola, C., Gross, C.T., and Ragozzino, D., 2015. Defective microglial development in the hippocampus of Cx3cr1 deficient mice. *Frontiers in Cellular Neuroscience*, 9 (March), 1–14.

Pagani, F., Testi, C., Grimaldi, A., Corsi, G., Cortese, B., Basilico, B., Baiocco, P., De Panfilis, S., Ragozzino, D., and Di Angelantonio, S., 2020. Dimethyl Fumarate Reduces Microglia Functional Response to Tissue Damage and Favors Brain Iron Homeostasis. *Neuroscience*, 439, 241–254.

Paolicelli, R.C., Bergamini, G., and Rajendran, L., 2019. Cell-to-cell Communication by Extracellular Vesicles: Focus on Microglia. *Neuroscience*, 405, 148–157.

Paolicelli, R.C., Bolasco, G., Pagani, F., Maggi, L., Scianni, M., Panzanelli, P., Giustetto, M., Ferreira, T.A., Guiducci, E., Dumas, L., Ragozzino, D., and Gross, C.T., 2011. Synaptic pruning by microglia is necessary for normal brain development. *Science*, 333 (6048), 1456–1458.

Paolicelli, R.C., Paolicelli, R.C., Bolasco, G., Pagani, F., Maggi, L., Scianni, M., Panzanelli, P., Giustetto, M., Ferreira, T.A., Guiducci, E., Dumas, L., Ragozzino, D., and Gross, C.T., 2014. Synaptic Pruning by Microglia Is Necessary for Normal Brain Development. *Science*, 1456 (2011), 10–13.

Paolicelli, R.C., Sierra, A., Stevens, B., Tremblay, M.E., Aguzzi, A., Ajami, B., Amit, I., Audinat, E., Bechmann, I., Bennett, M., Bennett, F., Bessis, A., Biber, K., Bilbo, S., Blurton-Jones, M., Boddeke, E., Brites, D., Brône, B., Brown, G.C., Butovsky, O.,

Carson, M.J., Castellano, B., Colonna, M., Cowley, S.A., Cunningham, C., Davalos, D., De Jager, P.L., de Strooper, B., Denes, A., Eggen, B.J.L., Eyo, U., Galea, E., Garel, S., Ginhoux, F., Glass, C.K., Gokce, O., Gomez-Nicola, D., González, B., Gordon, S., Graeber, M.B., Greenhalgh, A.D., Gressens, P., Greter, M., Gutmann, D.H., Haass, C., Heneka, M.T., Heppner, F.L., Hong, S., Hume, D.A., Jung, S., Kettenmann, H., Kipnis, J., Koyama, R., Lemke, G., Lynch, M., Majewska, A., Malcangio, M., Malm, T., Mancuso, R., Masuda, T., Matteoli, M., McColl, B.W., Miron, V.E., Molofsky, A.V., Monje, M., Mracsko, E., Nadjar, A., Neher, J.J., Neniskyte, U., Neumann, H., Noda, M., Peng, B., Peri, F., Perry, V.H., Popovich, P.G., Pridans, C., Priller, J., Prinz, M., Ragozzino, D., Ransohoff, R.M., Salter, M.W., Schaefer, A., Schafer, D.P., Schwartz, M., Simons, M., Smith, C.J., Streit, W.J., Tay, T.L., Tsai, L.H., Verkhratsky, A., von Bernhardi, R., Wake, H., Wittamer, V., Wolf, S.A., Wu, L.J., and Wyss-Coray, T., 2022. Microglia states and nomenclature: A field at its crossroads. *Neuron*, 110 (21), 3458–3483.

Parkhurst, C.N., Yang, G., Ninan, I., Savas, J.N., Yates, J.R., Lafaille, J.J., Hempstead, B.L., Littman, D.R., and Gan, W.B., 2013. Microglia promote learning-dependent synapse formation through brain-derived neurotrophic factor. *Cell*, 155 (7), 1596–1609.

Parnell, M., Guo, L., Abdi, M., and Cordeiro, M.F., 2012. Ocular manifestations of Alzheimer's disease in animal models. *International Journal of Alzheimer's Disease*, 2012.

Pérez-Cerdá, F., Sánchez-Gómez, M.V., and Matute, C., 2015. Pío del Río hortega and the discovery of the oligodendrocytes. *Frontiers in Neuroanatomy*, 9 (July), 7–12.

Perry, V.H., Nicoll, J.A.R., and Holmes, C., 2010. Microglia in neurodegenerative disease. *Nature Reviews Neurology*, 6 (4), 193–201.

Raivich, G., 2005. Like cops on the beat: The active role of resting microglia. *Trends in Neurosciences*, 28 (11), 571–573.

Reck-Peterson, S.L., Redwine, W.B., Vale, R.D., and Carter, A.P., 2018. The cytoplasmic dynein transport machinery and its many cargoes. *Nature Reviews Molecular Cell Biology*, 19 (6), 382–

398.

Reichert, F. and Rotshenker, S., 2019. Galectin-3 (MAC-2) controls microglia phenotype whether amoeboid and phagocytic or branched and non-phagocytic by regulating the cytoskeleton. *Frontiers in Cellular Neuroscience*, 13 (March), 1–9.

Renaud, C.C.N. and Bidère, N., 2021. Function of Centriolar Satellites and Regulation by Post-Translational Modifications. *Frontiers in Cell and Developmental Biology*, 9 (November), 1–8.

Rev, A., Dev, C., Downloaded, B., Wu, J., and Akhmanova, A., 2017. Microtubule-Organizing Centers.

Rivero, S., Cardenas, J., Bornens, M., and Rios, R.M., 2009. Microtubule nucleation at the cis-side of the golgi apparatus requires AKAP450 and GM130. *EMBO Journal*, 28 (8), 1016–1028.

Rosenbaum, J.T., Woods, A., Kezic, J., Planck, S.R., and Rosenzweig, H.L., 2011. Contrasting Ocular Effects of Local versus Systemic Endotoxin. *Investigative Ophthalmology and Visual Science*, 52 (9), 6472–6477.

Rosito, M., Deflorio, C., Limatola, C., and Trettel, F., 2012. CXCL16 orchestrates adenosine A 3 receptor and MCP-1/CCL2 activity to protect neurons from excitotoxic cell death in the CNS. *Journal of Neuroscience*, 32 (9), 3154–3163.

Rosito, M., Sanchini, C., Gosti, G., Moreno, M., De Panfilis, S., Giubettini, M., Debellis, D., Catalano, F., Peruzzi, G., Marotta, R., Indrieri, A., De Leonibus, E., De Stefano, M.E., Ragozzino, D., Ruocco, G., Di Angelantonio, S., and Bartolini, F., 2023. Microglia reactivity entails microtubule remodeling from acentrosomal to centrosomal arrays. *Cell Reports*, 42 (2), 112104.

Rusan, N.M., Fagerstrom, C.J., Yvon, A.M.C., and Wadsworth, P., 2001. Cell cycle-dependent changes in microtubule dynamics in living cells expressing green fluorescent protein-α tubulin. *Molecular Biology of the Cell*, 12 (4), 971–980.

Schindelin, J., Arganda-Carreras, I., Frise, E., Kaynig, V., Longair, M., Pietzsch, T., Preibisch, S., Rueden, C., Saalfeld, S., Schmid, B., Tinevez, J.Y., White, D.J., Hartenstein, V., Eliceiri, K., Tomancak, P., and Cardona, A., 2012. Fiji: An open-source

platform for biological-image analysis. *Nature Methods*, 9 (7), 676–682.

Schmittgen, T.D. and Livak, K.J., 2008. Analyzing real-time PCR data by the comparative CT method. *Nature Protocols*, 3 (6), 1101–1108.

Schroder, K. and Tschopp, J., 2010. The Inflammasomes. *Cell*, 140 (6), 821–832.

Seoane, P.I., Lee, B., Hoyle, C., Yu, S., Lopez-Castejon, G., Lowe, M., and Brough, D., 2020. The NLRP3-inflammasome as a sensor of organelle dysfunction. *The Journal of cell biology*, 219 (12), 1–12.

Sernagor, E., Eglen, S.J., and Wong, R.O.L., 2001. Development of retinal ganglion cell structure and function. *Progress in Retinal and Eye Research*, 20 (2), 139–174.

Shabab, T., Khanabdali, R., Moghadamtousi, S.Z., Kadir, H.A., and Mohan, G., 2017. Neuroinflammation pathways: a general review. *International Journal of Neuroscience*, 127 (7), 624–633.

Shintani, K., Ebisu, H., Mukaiyama, M., Hatanaka, T., Chinen, T., Takao, D., Nagumo, Y., Sakakura, A., Hayakawa, I., Usui, T., and Usui, T., 2020. Structure Optimization of Gatastatin for the Development of γ-Tubulin-Specific Inhibitor. *ACS Medicinal Chemistry Letters*, 11 (6), 1125–1129.

Sierra, A., Paolicelli, R.C., and Kettenmann, H., 2019. Cien Años de Microglía: Milestones in a Century of Microglial Research. *Trends in Neurosciences*, 42 (11), 778–792.

Ströhl, F. and Kaminski, C.F., 2015. A joint Richardson-Lucy deconvolution algorithm for the reconstruction of multifocal structured illumination microscopy data. *Methods and Applications in Fluorescence*, 3 (1), 14002.

Subhramanyam, C.S., Wang, C., Hu, Q., and Dheen, S.T., 2019. Microglia-mediated neuroinflammation in neurodegenerative diseases. *Seminars in Cell & Developmental Biology*, 94 (January), 112–120.

Tam, W.Y. and Ma, C.H.E., 2014. Bipolar/rod-shaped microglia are proliferating microglia with distinct M1/M2 phenotypes. *Scientific Reports*, 4, 1–7.

Tanaka, N., Meng, W., Nagae, S., and Takeichi, M., 2012.

Nezha/CAMSAP3 and CAMSAP2 cooperate in epithelial-specific organization of noncentrosomal microtubules. *Proceedings of the National Academy of Sciences of the United States of America*, 109 (49), 20029–20034.

Tarkowski, E., Andreasen, N., Tarkowski, A., and Blennow, K., 2003. Intrathecal inflammation precedes development of Alzheimer's disease. *Journal of Neurology, Neurosurgery and Psychiatry*, 74 (9), 1200–1205.

Tremblay, M.-E., Stevens, B., Sierra, A., Wake, H., Bessis, A., and Nimmerjahn, A., 2011. The Role of Microglia in the Healthy Brain. *Journal of Neuroscience*, 31 (45), 16064–16069.

Tremblay, M.Ě., Lowery, R.L., and Majewska, A.K., 2010. Microglial interactions with synapses are modulated by visual experience. *PLoS Biology*, 8 (11).

Turola, E., Furlan, R., Bianco, F., Matteoli, M., and Verderio, C., 2012. Microglial microvesicle secretion and intercellular signaling. *Frontiers in Physiology*, 3 MAY (May), 1–11.

Uhlemann, R., Gertz, K., Boehmerle, W., Schwarz, T., Nolte, C., Freyer, D., Kettenmann, H., Endres, M., and Kronenberg, G., 2016. Actin dynamics shape microglia effector functions. *Brain Structure and Function*, 221 (5), 2717–2734.

Valenzuela, A., Meservey, L., Nguyen, H., and Fu, M. meng, 2020. Golgi Outposts Nucleate Microtubules in Cells with Specialized Shapes. *Trends in Cell Biology*, 30 (10), 792–804.

Vertii, A., Ivshina, M., Zimmerman, W., Hehnly, H., Kant, S., and Doxsey, S., 2016. The Centrosome Undergoes Plk1-Independent Interphase Maturation during Inflammation and Mediates Cytokine Release. *Developmental Cell*, 37 (4), 377–386.

Vinogradova, T., Miller, P.M., and Kaverina, I., 2009. Microtubule network asymmetry in motile cells: Role of Golgi-derived array. *Cell Cycle*, 8 (14), 2168–2174.

Waites, C., Qu, X., and Bartolini, F., 2021. The synaptic life of microtubules. *Current Opinion in Neurobiology*, 69, 113–123.

Wang, M., Ma, W., Zhao, L., Fariss, R.N., and Wong, W.T., 2011. Adaptive Müller cell responses to microglial activation mediate neuroprotection and coordinate inflammation in the retina. *Journal of Neuroinflammation*, 8 (1), 173.

Webster, D.R. and Borisy, G.G., 1989. Microtubules are acetylated in domains that turn over slowly. *Journal of cell science*, 92 (Pt 1), 57–65.

Weigel, M., Wang, L., and Fu, M. meng, 2020. Microtubule organization and dynamics in oligodendrocytes, astrocytes, and microglia. *Developmental Neurobiology*, (October 2019), 1–11.

Wong, Y.L., Anzola, J. V., Davis, R.L., Yoon, M., Motamedi, A., Kroll, A., Seo, C.P., Hsia, J.E., Kim, S.K., Mitchell, J.W., Mitchell, B.J., Desai, A., Gahman, T.C., Shiau, A.K., and Oegema, K., 2015. Reversible centriole depletion with an inhibitor of Polo-like kinase 4. *Science*, 348 (6239), 1155–1160.

Wright, A.L., Zinn, R., Hohensinn, B., Konen, L.M., Beynon, S.B., Tan, R.P., Clark, I.A., Abdipranoto, A., and Vissel, B., 2013. Neuroinflammation and Neuronal Loss Precede Aβ Plaque Deposition in the hAPP-J20 Mouse Model of Alzheimer's Disease. *PLoS ONE*, 8 (4).

Wu, J. and Akhmanova, A., 2017. Microtubule-Organizing Centers. *Annual Review of Cell and Developmental Biology*, 33 (1), 51–75.

Wu, Y., Zheng, X., Ding, Y., Zhou, M., Wei, Z., Liu, T., and Liao, K., 2020. The molecular chaperone Hsp90α deficiency causes retinal degeneration by disrupting Golgi organization and vesicle transportation in photoreceptors. *Journal of Molecular Cell Biology*, 12 (3), 216–229.

Yang, X., Li, W., Zhang, S., Wu, D., Jiang, X., Tan, R., Niu, X., Wang, Q., Wu, X., Liu, Z., Chen, L., Qin, J., and Su, B., 2020. PLK 4 deubiquitination by Spata2-CYLD suppresses NEK7-mediated NLRP3 inflammasome activation at the centrosome . *The EMBO Journal*, 39 (2), 1–16.

Yau, K.W., vanBeuningen, S.F.B., Cunha-Ferreira, I., Cloin, B.M.C., vanBattum, E.Y., Will, L., Schätzle, P., Tas, R.P., vanKrugten, J., Katrukha, E.A., Jiang, K., Wulf, P.S., Mikhaylova, M., Harterink, M., Pasterkamp, R.J., Akhmanova, A., Kapitein, L.C., and Hoogenraad, C.C., 2014. Microtubule minus-end binding protein CAMSAP2 controls axon specification and dendrite development. *Neuron*, 82 (5), 1058–1073.

Yokoyama, M., Kobayashi, H., Tatsumi, L., and Tomita, T., 2022. Mouse Models of Alzheimer's Disease. *Frontiers in Molecular*

Neuroscience, 15 (June), 1–14.

Yu, Z., Yang, L., Yang, Y., Chen, S., Sun, D., Xu, H., and Fan, X., 2018. Epothilone B Benefits Nigral Dopaminergic Neurons by Attenuating Microglia Activation in the 6-Hydroxydopamine Lesion Mouse Model of Parkinson's Disease. *Frontiers in Cellular Neuroscience*, 12 (September), 1–13.

Zhu, X. and Kaverina, I., 2011. Quantification of asymmetric microtubule nucleation at subcellular structures. *Methods in Molecular Biology*, 777, 235–244.

Zimmerman, W.C., Sillibourne, J., Rosa, J., and Doxsey, S.J., 2004. Mitosis-specific Anchoring of γ Tubulin Complexes by Pericentrin Controls Spindle Organization and Mitotic Entry. *Molecular Biology of the Cell*, 15 (8), 3642–3657.

Acknowledgments